Enhanced ferroelectric and piezoelectric properties of BCT-BZT at the morphotropic phase boundary driven by the coexistence of phases with different symmetries

Smaranika Dash [iD],[1] Dhiren K. Pradhan,[2,3] Shalini Kumari,[4] Ravikant,[5] Md. Mijanur Rahaman [iD],[6] C. Cazorla [iD],[7]
Kumar Brajesh,[8] Ashok Kumar,[9,10] Reji Thomas [iD],[11,12] Philip D. Rack,[2,3] and Dillip K. Pradhan [iD][1,*]

[1]*Department of Physics and Astronomy, NIT Rourkela, Rourkela, Odisha 769008, India*
[2]*Department of Materials Science and Engineering, University of Tennessee, Knoxville, Tennessee 37996, USA*
[3]*Center for Nanophase Materials Sciences, Oak Ridge National Laboratory, Oak Ridge, Tennessee 37831, USA*
[4]*Department of Materials Science & Engineering, The Pennsylvania State University, University Park, Pennsylvania 16802, USA*
[5]*Department of Physics, Government College Sailana, Vikram University, Ujjain, Madhya Pradesh 456010, India*
[6]*Departmental of Materials Science and Engineering, University of Rajshahi, Rajshahi 6205, Bangladesh*
[7]*Departament de Física, Universitat Politècnica de Catalunya, Campus Nord B4-B5, Barcelona E-08034, Spain*
[8]*Department of Material Science and Engineering, Indian Institute of Technology Kanpur, Kanpur 208016, India*
[9]*CSIR-National Physical Laboratory, Dr. K. S. Krishnan Marg, New Delhi 110012, India*
[10]*Academy of Scientific and Innovative Research (AcSIR), Ghaziabad 201002, India*
[11]*Division of Research and Development, Lovely Professional University, Jalandhar-Delhi G.T. Road, Phagwara, Punjab 144411, India*
[12]*School of Chemical Engineering and Physical Sciences, Lovely Professional University, Jalandhar-Delhi G.T. Road, Phagwara,
Punjab 144411, India*

The discovery of lead-free piezoelectric materials is crucial for future information and energy storage applications. Enhanced piezoelectric and other physical properties are commonly observed near the morphotropic phase boundary (MPB) composition of ferroelectric solid solutions. The $(1-x)\mathrm{Ba(Zr_{0.2}Ti_{0.8})O_3}$-$x\mathrm{(Ba_{0.7}Ca_{0.3})TiO_3}$ (BZT-xBCT) system exhibits a large electromechanical response around its MPB region at $x = 0.5$. We report experimental and theoretical results of BZT-xBCT over a wide composition range $(0.3 \leqslant x \leqslant 1.0)$. X-ray diffraction and Raman spectroscopy studies indicate a composition-induced structural phase transition from a rhombohedral ($R3m$) phase at $x \leqslant 0.4$ to a tetragonal ($P4mm$) phase at $x \geqslant 0.6$ through a multiphase coexistence region at $0.45 \leqslant x \leqslant 0.55$ involving orthorhombic + tetragonal ($Amm2 + P4mm$) phases. First-principles calculations elucidate the phase competition in the coexistence region. The critical composition ($x = 0.5$) displays enhanced dielectric, ferroelectric, and piezoelectric properties, where notably $d_{33} \sim 320$ pC/N. This paper provides clear evidence of $Amm2 + P4mm$ crystallographic phases in the MPB region, which is responsible for the improved functional properties.

I. INTRODUCTION

Ferroelectric materials exhibit spontaneous and switchable electrical polarization, electro-optic, pyroelectric, and piezoelectric effects with strong electromechanical coupling [1,2]. This switchable polarization coupled with electronic transport properties, surface chemistry, and strain enables additional multifunctional device possibilities. Due to the existence of these functional properties, ferroelectric materials have attracted significant attention to both fundamental scientific interests and their potential applications in nonvolatile memory, energy storage, energy harvesting, transducers, actuators, motors, sensors, thermal imaging, and other multifunctional devices [2]. The current industries are dominated by Pb-based piezoelectric systems such as $\mathrm{Pb(Zr_xTi_{1-x})O_3}$ (PZT) ferroelectrics, $(1-x)\mathrm{Pb(Mg_{1/3}Nb_{2/3})O_3}$-$x\mathrm{PbTiO_3}$ (PMN $- x$PT) relaxors [1–4]. The lead-based ferroelectric/piezoelectric

systems are widely used in electromechanical devices due to their superior piezoelectric response. Most of the lead-based compounds contain >60 wt.% of toxic lead [2]. This hazardous toxic element is volatile in nature and released to the environment during processing. Thus, Pb recycling and disposal impose severe environmental and health concerns [3]. Policies have been enacted by various countries to restrict the use of toxic (Pb-based) materials in various electrical/electronic devices [4]. In addition, the volatility of lead during processing leads to nonstoichiometry and deterioration of the functional properties (like polarization, piezoelectric constants, and elastic constants) of devices [4,5]. In view of all these shortcomings, many research efforts are currently directed toward the discovery and design of lead-free materials with improved dielectric, ferroelectric, and piezoelectric properties. Some of the promising lead-free candidates are $\mathrm{BaTiO_3}$ (BT)-, $\mathrm{K_{1-x}Na_xNbO_3}$ (KNN)-, and $\mathrm{Bi_{1/2}Na_{1/2}TiO_3}$ (NBT)-based materials [2,3]. Among them, KNN and NBT contain volatile elements like Bi, Na, and K, which result in off-stoichiometry and poor densification that lead to

*dillip.pradhan79@gmail.com

degradation of physical properties [5]. Although BT is one of the important ferroelectric oxides, it possesses a relatively low piezoelectric coefficient ($d_{33} \sim 200$ pC/N), which limits the device applications [6]. However, doped/modified BT-based materials have received significant attention in recent years after the discovery of Ca- and Zr-doped BT, i.e., $(1-x)\mathrm{Ba(Zr_{0.2}Ti_{0.8})O_3}$-$x(\mathrm{Ba_{0.7}Ca_{0.3})TiO_3}$ (BZT-xBCT) for $x = 0.5$, which exhibits giant piezoelectric response $d_{33} \sim 620$ pC/N and exceeds that of many soft PZT-based materials [7].

$\mathrm{BaTiO_3}$ undergoes a sequence of structural phase transitions with temperature. With decreasing temperature, the paraelectric cubic phase $Pm\overline{3}m$ transforms to the ferroelectric tetragonal ($P4mm$) phase at $\sim 130\,^\circ\mathrm{C}$, and $<130\,^\circ\mathrm{C}$, the material remains in the ferroelectric state. Around $0\,^\circ\mathrm{C}$, the tetragonal ($P4mm$) phase changes to an orthorhombic ($Amm2$) phase, and $\sim -90\,^\circ\mathrm{C}$, this orthorhombic phase changes to a rhombohedral ($R3m$) phase. These two ferroelectric transitions are of first order in nature [3]. By doping/chemical modifications, different ferroelectric phases can be created in BT. In the case of ferroelectric solid solutions, compositional modifications can induce a structural transformation from one ferroelectric state to another state having different crystal symmetry. This structural instability is termed as inter-ferroelectric instability [8]. This interferroelectric instability lowers the energy barrier that separates the two ferroelectric phases, and it provides an easy path for the polarization rotation. Consequently, enhanced ferroelectric and piezoelectric response are typically observed around morphotropic phase boundary (MPB) compositions in ferroelectric solid solutions [9–12]. Hence, tailoring the physical properties in ferroelectric materials by inducing MPB compositions is an interesting approach for the BT system. The 0.5BZT-0.5BCT system has been actively studied for the replacement of Pb-based ferroelectrics for device applications. However, the mechanisms responsible for the exceptionally high piezoelectric properties are still not fully understood.

The enhanced piezoelectric and ferroelectric properties in the BZT-xBCT systems have been investigated from the structural perspective, and the origin of the enhancement has been explained by different theories and models (see Table SI in the Supplemental Material for a detailed table summarizing previous structural studies [13]; see also Refs. [7,14–49]). The first phase diagram on this solid solution was reported by Liu and Ren [7], where the MPB with a triple point consisting of cubic $Pm\overline{3}m$, rhombohedral ($R3m$), and tetragonal ($P4mm$) crystallographic phases was proposed. The enhanced piezoresponse was explained for the MPB composition due to this tricritical point, which led to a vanishing polarization anisotropy that facilitates the polarization rotation between tetragonal and rhombohedral phases [7]. The phase coexistence of rhombohedral and tetragonal phase composition was verified experimentally by Ehmke *et al.* [17] and Haugen *et al.* [26] based on high-resolution synchrotron x-ray diffraction (XRD). This observation was confirmed by Gao *et al.* [29] using convergent beam electron diffraction analysis. The phase diagram was further reinvestigated by Keeble *et al.* [20], using high-resolution synchrotron XRD, and they reported the existence of an intermediate orthorhombic phase between the rhombohedral and tetragonal phases, which was supported by Tian *et al.* [27] as well. Based on these

findings, it was suggested that phase coexistence regions are the convergent regions instead of the tricritical point, as reported by Liu and Ren [7]. In a ferroelectric system, the region in the phase diagram where different phase boundaries (for example, cubic-tetragonal, tetragonal-orthorhombic, and orthorhombic-rhombohedral) converge is referred to as the *convergent region* [20]. The enhanced piezoelectric properties were attributed to the presence of the orthorhombic phase. Contrary to these reports, Acosta *et al.* [50] reported that neither the triple point nor the phase convergence region can explain the enhanced piezoelectric properties in the BZT-BCT system. Further, Gao *et al.* [51] posited that the enhanced piezoelectric response is due to the reversible domain wall motion in the BZT-BCT system based on the small field Rayleigh analysis and large field strain measurements. Tutuncu *et al.* [31] studied the origin of enhancement of the piezoresponse in BZT-xBCT solid solutions using electric field-dependent *in situ* XRD analysis and showed the presence of a $90\,^\circ$ domain wall. The enhancement of electrochemical response and piezoelectric properties in BZT-xBCT was then attributed to this $90\,^\circ$ domain wall.

A high-resolution *in situ* transmission electron microscopy (TEM) study on the electrical poling-driven structural transformation from the $R3m + P4mm$ to the $Amm2$ phase of a single domain of BZT-BCT system was performed by Guo *et al.* [33]. The primary contribution of structural instabilities along with the elastic softening due to the initial electrical poling-repoling was found to be responsible for the enhanced piezoelectric properties [33]. Recently, Brajesh *et al.* [34] studied the electric field and temperature-driven structural phase transformation based on XRD analysis on 0.5BZT-0.5BCT and reported the coexistence of three phases: tetragonal ($P4mm$) + orthorhombic ($Amm2$) + rhombohedral ($R3m$) at room temperature. They argued that the presence of structural heterogeneity gives rise to polar nanoregions (PNRs) as in the case of relaxor ferroelectric systems. Due to the presence of the PNRs, field-induced transformation and domain wall motion occur, which were ascribed to the amplification of the piezoresponse. Based on the combined theoretical and experimental investigations, Acosta *et al.* [52] also reported that the enhanced piezoelectric properties originate at the phase boundary of the orthorhombic-tetragonal phase, due to reduced anisotropy energy, high polarization, and elastic softening. Further, the structural investigation confirmed the presence of the orthorhombic phase between rhombohedral and tetragonal phases [52]. Based on large-scale atomistic simulations, Nahas *et al.* [53] reported the existence of large polarization fluctuations in the orthorhombic phase due to the combined effect of flat free energy landscape, the fragmented local structure, and the stability of the orthorhombic phase for a narrow temperature range. This polarization fluctuation/rotation through the orthorhombic (low symmetry) phase is responsible for the enhanced piezoresponse in the BZT-xBCT system [53]. Akbarzadeh *et al.* [43] investigated the phase diagram of BZT-xBCT systems numerically using the classical Monte Carlo simulations and path integral Monte Carlo simulations. They observed a quantum fluctuation-induced orthorhombic phase and suggested the enhancement of the piezoelectric properties is due to the inhomogeneous local structure. Zhang *et al.*

[39] suggested the relaxorlike behavior in the BZT-xBCT system is due to cation substitution of different ionic radii (at A and B sites), which creates heterogeneous strain at a local length scale. This local strain heterogeneity influences the elastic behavior near the MPB and results in an adaptive nanoscale microstructure, which in turn enhances the piezoelectric response [39]. Recently, Mondal *et al.* [47] studied pressure-dependent XRD on 0.5BZT-0.5BCT composition and showed a mixed orthorhombic (*Amm*2) + tetragonal (*P4mm*) phase at room temperature. Datta *et al.* [54] reported the mechanism of enhancement of piezoelectric properties based on total neutron scattering and Raman scattering and presented a statistical description of the atomic level polar ordering in the BZT-xBCT system. The enhancement of the piezoresponse was described in terms of the increased interaction among the cations in a strained local environment. They also proposed that the presence of low-symmetry crystal structures cannot be a universal concept for the enhancement of piezoelectric response in any ferroelectric solid solution around the MPB [54].

Despite the wide range of experimental and theoretical investigations on the BZT-xBCT system, a clear picture has not been developed to explain the coexistence of the crystal structures and enhanced piezoelectricity around the MPB. Hence, it is very important to understand the mechanism behind the exceptional piezoelectric properties of lead-free BZT-xBCT. A fundamental understanding of the structure-property relationships in BZT-xBCT near the MPB region is necessary, both from experimental and theoretical points of view. To better understand the structure-property relationships (i.e., composition-driven structural phase transitions) in BZT-xBCT, a systematic investigation on the structure-driven phase transition of BZT-xBCT ($0.3 \leqslant x \leqslant 1.0$) is studied. XRD and Raman scattering studies on the composition-induced structural phase transitions are expected to elucidate evidence of the MPB region. Additionally, first-principles calculations based on density functional theory (DFT) were performed to theoretically describe phase competition in the multiphase system. Furthermore, we measure and correlate the enhancement of the dielectric, ferroelectric, and piezoelectric properties with the crystal structure around the MPB region and discuss the relaxor behavior of the system.

II. EXPERIMENTAL DETAILS

Polycrystalline ceramics of $(1 - x)$Ba(Zr$_{0.2}$Ti$_{0.8}$)O$_3$ -x(Ba$_{0.7}$Ca$_{0.3}$)TiO$_3$ (BZT-xBCT) with $x = 0.3$, 0.4, 0.45, 0.48, 0.5, 0.52, 0.55, 0.6, 0.7, 0.8, 0.9, and 1.0 were prepared using the autocombustion technique. Stoichiometric amounts of high-purity Ba(NO$_3$)$_2$, Ca(NO$_3$)$_2$4H$_2$O, ZrO(NO$_3$)$_2$xH$_2$O, Ti[OCH(CH$_3$)$_2$]$_4$, and urea were taken as raw materials for the synthesis. The urea was used as fuel and above raw materials forms the oxidizer. The above precursors were mixed stoichiometrically for the desired composition with a minimum amount of distilled water while maintaining the fuel : oxidizer ratio of 1. The detailed synthesis procedure was described elsewhere [55]. The samples were then calcined at 900 °C for 6 h. The calcined powder was then mixed with 3 wt. % polyvinyl alcohol and pressed to form disks of 10 mm diameter at a pressure of 6×10^7 kg/m^2. The green pellets

were initially heated at 600 °C for 1 h to remove the binder and finally sintered at an optimized temperature of 1450 °C for 4 h.

Room-temperature XRD data were collected using a high-resolution x-ray diffractometer, (PANalytical X'Pert Pro MPD), with Cu K$_\alpha$ radiation ($\lambda = 1.5405$ Å). For the XRD measurement, sintered pellets were crushed into fine powders and sieved followed by a heat treatment at 600 °C for 2 h to release the intergranular stress present in the sample during the grinding process. Rietveld refinements of the XRD patterns were carried out using FULLPROF software package. The room-temperature Raman spectra of the sintered samples were recorded by a Raman spectrometer (Horiba Jobin Yvon T64000 system) using a 532 nm laser in the frequency range of $10-1000$ cm^{-1}. The surface morphology of the samples was recorded using a field emission scanning electron microscope (FESEM; NOVA Nano SEM 450). Sintered pellets were coated with gold for collecting the SEM micrographs to minimize charging. The presence of different elements along with the elemental composition ratio was studied with the help of energy dispersive x-ray spectroscopy (EDX) attached to FESEM equipment. For electrical measurements, both sides of the pellets were coated with silver paint and further dried at 200 °C for 2 h. The dielectric properties were measured at a temperature range from room temperature to 500 °C in the frequency range of 100 Hz to 1 MHz using an impedance analyzer (HIOKI IM3570) with an oscillating voltage of 1 V. The room-temperature ferroelectric hysteresis loops (*P-E*) were collected using a ferroelectric loop tester (Radiant Ferroelectric Tester) at a frequency of 10 Hz. The silver-electroded samples were subjected to electrical poling at an applied DC electric field of 20 kV/cm at room temperature in a silicon oil bath before the *P-E* loop measurement. The piezoelectric coefficient (d_{33}) was measured using a YE2730A d_{33} meter after electrical poling.

The energetic and structural properties of lead-free BZT-xBCT ceramics were calculated with first-principles methods based on DFT. We used the PBE variant of the generalized gradient approximation to DFT [56] as it is implemented in the VASP package [57,58]. The projector augmented wave method was employed to represent the ion cores [59], and we considered the following valence electrons: Ba 5s, 5p, and 6s; Ca 3s, 3p, and 4s; Ti 3p, 4s, and 3d; Zr 4s, 4p, 5s, and 4d; and O 2s and 2p. Wave functions were represented in a plane-wave basis truncated at 650 eV. We used a 40-atom simulation cell (equivalent to a $2 \times 2 \times 2$ replication of the typical 5-atom perovskite unit cell in which the usual ferroelectric and antiferrodistortive distortions occurring in oxide compounds could be reproduced [60–63]. For integrations within the first Brillouin zone, we adopted a Γ-centered k-point grid of $6 \times 6 \times 6$. Geometry relaxations were performed by using a conjugate-gradient algorithm that optimized the volume and shape of the simulation cell as well as the atomic positions. The imposed tolerance on the atomic forces was of 0.01 eV Å^{-1}. By using these parameters, we obtained total energies that were converged to within 0.5 meV per f.u. To provide meaningful comparisons with the experiments, in our DFT calculations, we considered four different system compositions: Ba$_6$Ca$_2$Ti$_8$O$_{24}$ (referred to as $x = 1.00$), Ba$_7$Ca$_1$Ti$_7$Zr$_1$O$_{24}$ (referred to as $x = 0.50$), Ba$_7$Ca$_1$Ti$_6$Zr$_2$O$_{24}$ (referred to as

$x \approx 0.50$), and $Ba_8Ti_6Zr_2O_{24}$ (referred to as $x = 0.00$). Four different polymorphs were analyzed for each composition, namely, tetragonal (polar, space group *P4mm*), cubic (non-polar, space group $Pm\bar{3}m$), rhombohedral (polar, space group *R3m*), and orthorhombic (polar, space group *Amm*2).

III. RESULTS

A. XRD

Figure 1 represents the compositional evolutions of the XRD profile for the five pseudocubic (pc) reflections $\{0\,0\,1\}_{pc}$, $\{1\,1\,1\}_{pc}$, $\{2\,0\,0\}_{pc}$, $\{2\,2\,2\}_{pc}$, and $\{4\,0\,0\}_{pc}$ for the entire composition range of BZT-*x*BCT ferroelectric materials. The XRD profiles presented here contain $K\alpha_2 (= 1.54439\,\text{Å})$ reflections apart from the main $K\alpha_1 (\lambda = 1.5405\,\text{Å})$ reflection. The distinct change in the pc reflections suggests a composition-induced structural phase transition. The Rietveld refinement analysis was carried out to ascertain the exact nature of this structural phase transition, and the starting model for the refinement was proposed based on a visual analysis of the XRD spectra. Scrutiny of the splitting of the characteristic pc reflections $\{h00\}_{pc}$, $\{hh0\}_{pc}$, and $\{hhh\}_{pc}$ is the best way to identify the presence of tetragonal, orthorhombic, and rhombohedral phases. All the pc reflections are singlet for cubic symmetry. For the tetragonal crystal structure, the pc reflections are characterized by the splitting of the $\{h00\}_{pc}$ reflection into doublets, and $\{hhh\}_{pc}$ appears to be singlet. However, in the case of the rhombohedral crystal structure, the reverse behavior is expected, i.e., $\{hhh\}_{pc}$ reflections are doublets, and $\{h00\}_{pc}$ reflections are singlet. In the case of the orthorhombic crystal structure, splitting of both $\{hhh\}_{pc}$ and $\{h00\}_{pc}$ reflections is expected. Weak distortions in the structure are difficult to visualize in the lower order reflections (at lower angles), and hence, higher order reflections (at higher angles) were considered. However, the intensity of higher order reflections is considerably weaker than the lower order reflections. In the present case, the peak-to-background ratio and resolution of our diffraction data are sufficient to identify different crystallographic phases (tetragonal, orthorhombic, and rhombohedral) explicitly.

The singlet nature of the $\{1\,1\,1\}_{pc}$ reflections and doublet nature of the $\{2\,0\,0\}_{pc}$ reflection suggest the tetragonal crystal structure for $x = 1.0$. Detailed information can be obtained by carefully analyzing the higher order reflections, so reflections such as $\{2\,2\,2\}_{pc}$ and $\{4\,0\,0\}_{pc}$ are also plotted and shown in Fig. 1. For pure BCT ($x = 1.0$), the doublet nature of the $\{4\,0\,0\}_{pc}$ reflection and singlet $\{2\,2\,2\}_{pc}$ reflection confirm the tetragonal crystal structure with space group *P4mm*. With an increase in the BZT concentration, the doublet $\{4\,0\,0\}_{pc}$ and singlet $\{2\,2\,2\}_{pc}$ reflection are maintained up to $x = 0.60$. Thus, the XRD data were fitted using a Rietveld refinement technique with a single-phase *P4mm* crystal structure ($0.6 \leqslant x \leqslant 1.0$), and a representative Rietveld refinement pattern for $x = 1.0$ is shown in Fig. 2(a). To have better clarity, we have compared the fitted data for higher order reflections, which are shown as an inset of Fig. 2. There is good agreement between the experimental and the fitted data. The refined structural parameters obtained from Rietveld refinement for $x = 1.0$ are shown in Table SII in the Supplemental Material [13].

With an increase in the concentration of BZT, there is a distinct change in the pc diffraction pattern for $x = 0.55$ and then for $x = 0.40$ (Fig. 1). Thus, based on visual inspection of the pc diffraction pattern, there are distinct structures for the composition ranges $0.3 \leqslant x \leqslant 0.4$, $0.45 \leqslant x \leqslant 0.55$, and $0.6 \leqslant x \leqslant 1.0$. For the composition $x = 0.3$ and 0.4, the pc $\{4\,0\,0\}_{pc}$ profile is singlet (Fig. 1), which suggests the presence of rhombohedral (*R3m*) rather than tetragonal or orthorhombic phases.

Further, Rietveld refinements of the XRD patterns for $x = 0.4$ with both *R3m* and *Amm*2 space groups has been carried out [Figs. 2(d) and 2(e)], where the best fitting is observed for the *R3m* space group, confirming rhombohedral structure for this compositional range. However, for $x = 0.55$, the Rietveld refinement using the *P4mm* space group resulted in a poor fit, as the shape of the $\{4\,0\,0\}_{pc}$ reflection is significantly modified due to the appearance of a new peak in between the two tetragonal peaks. Indeed, $\{4\,0\,0\}_{pc}$ reflections of both the *Amm*2 and *P4mm* structures are doublets. Thus, the presence of the extra reflections along with the *P4mm* tetragonal phase suggests the coexistence of those two phases in the $x = 0.55$ composition. The pc $\{4\,0\,0\}_{pc}$ reflections of the tetragonal phase, namely, $(004)_T$ and $(400)_T$, show doublets at the extreme ends. As can be seen from Fig. 2, along with the doublet nature for the tetragonal distortions, the presence of peaks in the middle (between the tetragonal peaks) correspond to the orthorhombic structure (marked as O). It has been observed that the intensity of the orthorhombic (*Amm*2) phase increases with a decrease in the BCT concentrations from $x = 0.55$ to 0.45. The increasing intensity of the orthorhombic peak in between the tetragonal peak confirms the increasing fraction of the *Amm*2 phase.

Since some of the peaks are not fit with *P4mm* structure for $x = 0.55$, a different coexistent structural model was considered. Here, pure BCT ($x = 1.0$) to BZT-*x*BCT ($x = 1.0$ to 0.6) crystalizes in the *P4mm* crystal structure, whereas $x = 0.3$ and 0.4 belong to the rhombohedral crystal structure (*R3m*). Since the composition $x = 0.55$ is expected to be the crossover from *P4mm* to *P4mm* + *Amm*2, different models: (i) single-phase tetragonal (*P4mm*) structure, (ii) single-phase orthorhombic (*Amm*2) structure, (iii) tetragonal (*P4mm*) + rhombohedral (*R3m*) structure, and (iv) tetragonal (*P4mm*) + orthorhombic (*Amm*2) structure were fit to the powder XRD data using a Rietveld refinement. In the case of the BT-based ferroelectric system, the identification of the rhombohedral and orthorhombic phases is difficult due to similar pc lattice parameters [36].

The fitted results for the *P4mm* + *R3m* and *P4mm* + *Amm*2 coexistence model are shown in Figs. 2(b) and 2(c) for $x = 0.55$. The insets of the figure show the magnified fitted plot of higher angle pc reflections $\{2\,0\,0\}_{pc}$, $\{2\,2\,2\}_{pc}$, and $\{4\,0\,0\}_{pc}$. The subtle misfit regions (indicated by an arrow mark in the magnified pc $\{2\,0\,0\}_{pc}$ and $\{0\,0\,4\}_{pc}$ reflections) are observed for the refined *P4mm* + *R3m* phases for $x = 0.55$. Among the different structural model, the tetragonal and orthorhombic (*P4mm* + *Amm*2) coexistence model gives the best fit. The refined structural parameters obtained from Rietveld refinement for $x = 0.55$ are shown in Table SIII in the Supplemental Material [13]. Due to the addition of *Amm*2 to the *P4mm* model, the software attempts to obtain the best
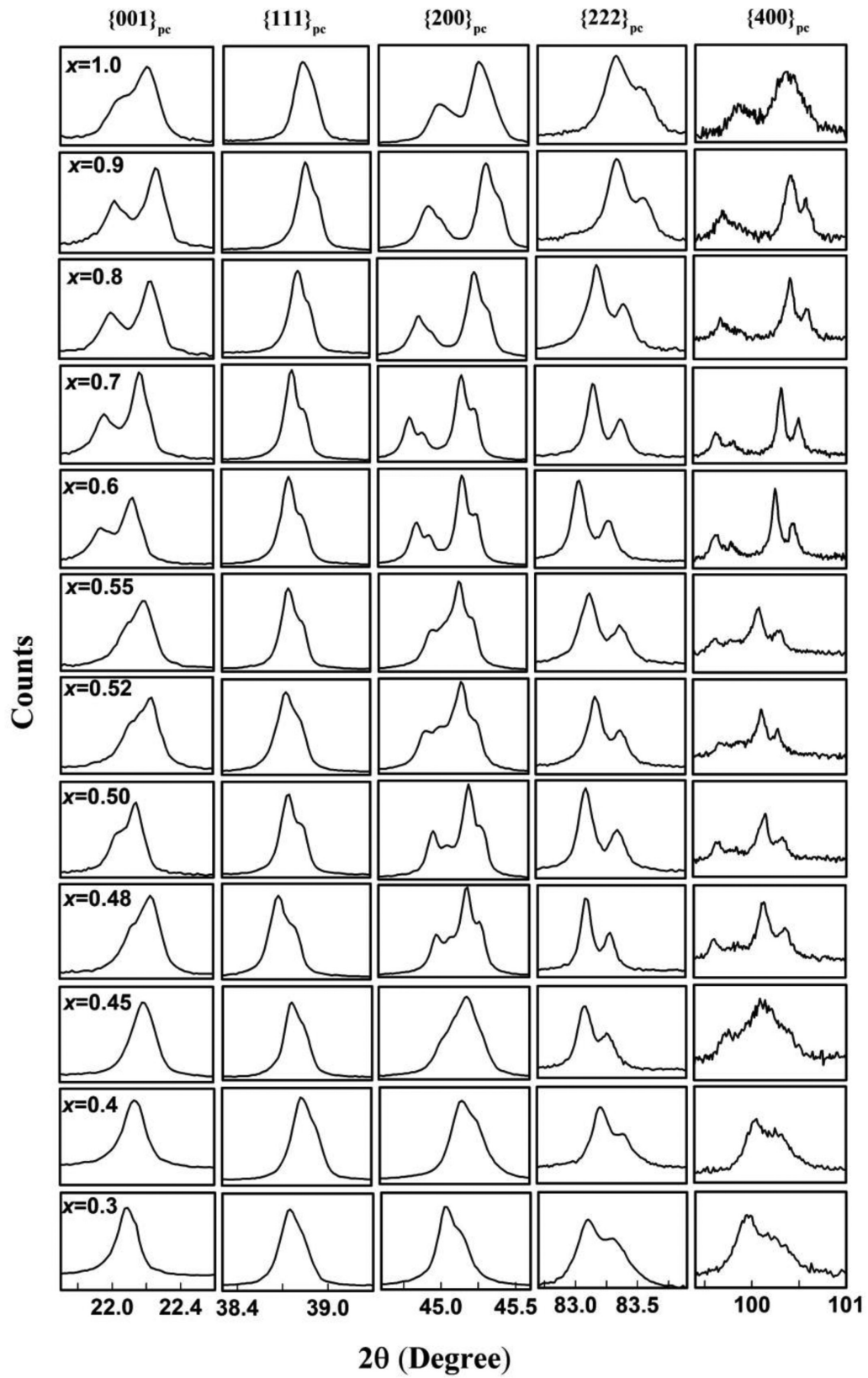
FIG. 1. Evolution of pseudocubic Bragg profiles of $\{0\,0\,1\}_{pc}$, $\{1\,1\,1\}_{pc}$, $\{2\,0\,0)_{pc}$, $\{2\,2\,2\}_{pc}$, and $\{4\,0\,0\}_{pc}$ obtained from room-temperature x-ray powder diffraction of BZT-xBCT with $0.3 \leqslant x \leqslant 1.0$.
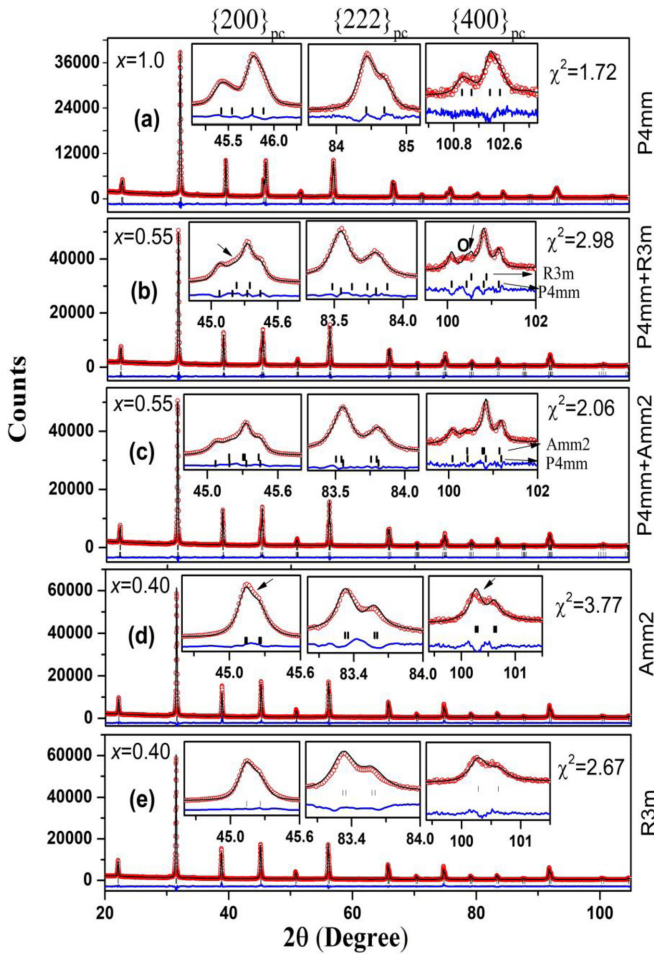
FIG. 2. Rietveld refined x-ray diffraction (XRD) pattern of BZT-*x*BCT for (a) $x = 1.0$ using the $P4mm$ model (b) and (c) $x = 0.55$ using the $P4mm + R3m$ and $P4mm + Amm2$ model, and (d) and (e) $x = 0.4$ using the $Amm2$ and $R3m$ model. The inset shows the enlarged view of the high quality of fit with selected Bragg profiles.

fit by increasing the width of the Bragg peaks. This way, additional intensity due to another phase is compensated. Thus, the $P4mm + Amm2$ phase coexistence model was extended up to $x = 0.45$, and a best fit was observed. In short, the coexistence of the $P4mm$-$Amm2$ ferroelectric crystallographic phases is the best way to explain the appearance of the orthorhombic phase along with the tetragonal phase, as observed in the XRD pattern (i.e., triplet nature of $\{2\,0\,0\}_{pc}$ and $\{4\,0\,0\}_{pc}$ diffraction profiles). Although, the visual observation suggests that $x = 0.4$ is the rhombohedral crystal structure, we have fitted with both the orthorhombic and rhombohedral crystal structures. The $x = 0.40$ Rietveld refinement revealed a very poor fit of the $\{4\,0\,0\}_{pc}$, $\{2\,0\,0\}_{pc}$, and $\{2\,2\,2\}_{pc}$ reflections with the $Amm2$ phase. Dramatic improvements in the fitting occur when considering the $R3m$ rhombohedral structure. The refined structural parameters obtained from Rietveld refinement for $x = 0.4$ are shown in Table SIV in the Supplemental Material [13]. The Rietveld refinement on the XRD analysis reveals that BZT-*x*BCT exhibits the single-phase $P4mm$ crystal structure in the regions $1.0 \leqslant x \leqslant 0.6$, the coexistence of the $P4mm + Amm2$ structure for the composition range

$0.55 \leqslant x \leqslant 0.45$, and another single phase in the composition range $0.3 \leqslant x \leqslant 0.4$ with $R3m$ crystal structure. The phase coexistence model has been critically studied by plotting the variation of pc lattice parameters, unit cell volume, and phase fraction obtained from Rietveld refinement, as shown in Fig. S1 in the Supplemental Material [13]. First, we have converted the orthorhombic lattice parameter (a, b, c) into an equivalent perovskite pc lattice parameter using the following relation $a_{pc} = a$, $b_{pc} = b/\sqrt{2}$, $c_{pc} = c/\sqrt{2}$, where a_{pc}, b_{pc}, and c_{pc} represent the lattice parameters for the strain-free cubic lattice [64]. The obtained values of b_{pc} and c_{pc} are nearly same, and both are larger than a_{pc}, so we introduce a term $c_{avg} = (b_{pc} + c_{pc})/2$.

For better representation, we have plotted the whole composition range into three different regions, i.e., region I, $x = 0.3 - 0.4$ (rhombohedral $R3m$ phase); region II, $x = 0.45 - 0.55$ (coexistence of $P4mm + Amm2$) phase; and region III, $x = 0.6 - 1.0$ (tetragonal $P4mm$ phase), shown in Fig. S1 in the Supplemental Material [13]. In region I, i.e., at higher concentration of BZT, the rhombohedral ($R3m$) lattice parameter (a_R) is relatively high. The pc lattice parameters in both region I (corresponds to single-phase rhombohedral structure with space group $R3m$) and region III (corresponds to single-phase tetragonal structure with space group $P4mm$) decrease with the increase in BCT concentration. The decrease in the lattice parameter is due to the large ionic radius of Zr^{4+} as compared with Ti^{4+}. Similarly, the unit cell volume/formula unit also decreases with the increase in the BCT concentrations both in region I and region III. However, in the phase coexistence region (region II), the pc lattice parameters a_{pc} and c_{pc} correspond to the orthorhombic structure, and the tetragonal lattice parameters a_T and c_T decrease slightly with increase in the BCT concentration up to $x = 0.5$, and these values increase with further increase in BCT concentrations. Similarly, the unit cell volume also shows a discontinuous change (change of slope) of its value around the phase coexistence region. For the compositions $x = 0.3$ and 0.4, the structure corresponds to purely rhombohedral ($R3m$; i.e., 100% rhombohedral phase fraction). However, for $0.45 \leqslant x \leqslant 0.55$, i.e., in region II, a phase coexistence of $Amm2$ and $P4mm$ is obtained. For $x = 0.45$, the volume fractions of $Amm2$ and $P4mm$ are found to be 61 and 39%, respectively. With the increase in BCT concentration, the phase fraction of $Amm2$ drops to 18%, while that of $P4mm$ rises to 82% for $x = 0.55$, and above that, i.e., $0.6 \leqslant x \leqslant 1.0$, it exhibits purely a tetragonal ($P4mm$) structure. The discontinuous changes in the unit cell volume and phase coexistence of two different crystallographic phases in the phase coexistence regions ($0.45 \leqslant x \leqslant 0.55$) indicate the first-order phase transitions from $R3m$ (rhombohedral) to $P4mm$ (tetragonal) through the $Amm2 + P4mm$ phases [65].

B. Raman spectroscopy

Raman spectroscopy is a nondestructive probe of the structure of ferroelectric materials owing to its sensitivity to local symmetry. Raman scattering also provides information about local heterogeneities related to compositional and structural disorder because of the shorter coherence length and time scale of phonons. Therefore, the Raman spectra of the BZT-*x*BCT system have been studied as a function of

composition for realizing BCT doping effects to local heterogeneity structure of BZT-xBCT ceramics. The reduced intensity $I^r(\omega)$, corrected for the Bose-Einstein phonon population, was reckoned from Stokes components of observed Raman scattering intensity $I(\omega)$ as follows [66,67]:

$$I^r(\omega) = \frac{I(\omega)}{\omega[n(\omega)+1]}, \tag{1}$$

where $n(\omega) = 1/[\exp(\hbar\omega/k_BT)-1]$ represents the Bose-Einstein population factor. Here, $\hbar$ and k_B indicate Dirac and Boltzmann constants, respectively. To understand the BCT doping effects on BZT-xBCT, all reduced Raman spectra in the frequency range of 50–100 cm^{-1} were fitted by combining a Lorentzian central peak (CP), damped harmonic oscillator model, and a Fano function as follows [66,67]:

$$I^r(\omega) = \frac{2A_{CP}}{\pi} \frac{\Gamma_{CP}}{4\omega^2 + \Gamma_{CP}^2} + \sum_i \frac{A_i \Gamma_i \omega_i^2}{(\omega^2 - \omega_i^2)^2 + \omega^2 \Gamma_i^2}$$
$$+ \frac{I_0(q+\varepsilon)^2}{(1+\varepsilon)^2}, \tag{2}$$

where A_{CP} and Γ_{CP} indicate the intensity and full width at half maximum (FWHM) of the CP, respectively, which are related to the relaxation process of precursor dynamics. Here, A_i, ω_i, and Γ_i represent intensity, frequency, and damping constant of the ith optical Raman active mode, respectively. The I_0 is the Fano resonance intensity, q reflects the asymmetry parameter representing the coupling strength between a continuum state and a discrete phonon, and $\varepsilon = 2(\omega - \omega_{A1(1TO)})/\Gamma_{A1(1TO)}$ denotes reduced energy, where $\Gamma_{A1(1TO)}$ is the FWHM of the Fano resonance. The fitted Raman spectra using Eq. (2) are displayed in Fig. 3(b).

The composition-dependent Raman spectra measured at room temperature of the BZT-xBCT is shown in Fig. 3(a). The observed Raman spectra exhibit a similar profile of the pure BaTiO$_3$ (BT) [68]. Therefore, the effective vibrational modes of BZT-xBCT ceramics are like that of pure BT. Pure BT is a typical ferroelectric material, and it has tetragonal structure at room temperature. In the paraelectric cubic phase, the Raman modes of BT transform as the $3T_{1u} + T_{2u}$ irreducible presentations of the $Pm\bar{3}m$ symmetry. The F_{2u} mode is silent, and F_{1u} modes are only infrared active. Therefore, the Raman activity is not allowed in the paraelectric phase with perfect cubic symmetry.

A ferroelectric tetragonal phase with $P4mm$ symmetry has $3A_1$ and $3E$ modes, which come from infrared active F_{1u} modes, and one silent $E + B_1$ mode arises from the F_{2u} mode. Each of the A_1 and E modes splits into transverse optic (TO) and longitudinal optic (LO) modes due to long-range electrostatic forces associated with lattice ionicity. The detailed mode symmetry assignments of BaTiO$_3$ are reported elsewhere [69–71].

As can be seen in Figs. 3(b) and 3(c), the Raman spectrum in the frequency range of 50–1000 cm^{-1} of the BZT-xBCT ($x = 0.30$) consists of mainly $A_1(1TO)$ ($\sim$117 cm^{-1}), $A_1(1LO)$ ($\sim$140 cm^{-1}), $E(2TO)$ ($\sim$189 cm^{-1}), $A_1(2TO)$ ($\sim$261 cm^{-1}), $E(3TO)/E(1LO)/B_1$ ($\sim$297 cm^{-1}), $E(4TO)$ ($\sim$512 cm^{-1}), $A_1(3TO)$ ($\sim$528 cm^{-1}), $E(3LO)$ ($\sim$717 cm^{-1}), and $A_1(2LO)$ ($\sim$744 cm^{-1}). In BZT-xBCT ($x = 0.3$), the broad peak at $\sim$330 cm^{-1} may correspond to silent mode,

which comes from higher order processes [72]. However, the weak mode $\sim$630 cm^{-1} [Fig. 3(c)] may be due to lattice disorder, which was attributed to mismatch of ionic radii at crystallographically equivalent sites [73]. At room temperature, the main spectral features observed in BZT-xBCT ceramics are a Fano-like asymmetric $A_1(1TO)$ mode, a symmetric $A_1(1LO)$ mode, a symmetric broad $E(2TO)$ mode, an asymmetric broad $A_1(2TO)$ mode, a sharp $E(3TO)/E(1LO)/B_1$ mode, symmetric intense $E(4TO)$, $A_1(3TO)$, and $E(3LO)$ modes, and a symmetric broad intense $A_1(2LO)$ mode, as shown in Figs. 3(b) and 3(c). The intense $A(1TO)$, $A_1(2TO)$, $E(3TO)/E(1LO)/B_1$, $E(4TO)/A_1(3TO)$, and $E(3LO)/A_1(2LO)$ modes correspond to the tetragonal phase of the pure BT [68]. An additional intense mode at $\sim$189 cm^{-1} is observed in BZT-xBCT ($x = 0.30$) in addition to phonon modes assigned to the tetragonal phase, as shown in Figs. 3(a) and 3(b). The peak position of this mode shifted to the higher wave number up to $\sim$202 cm^{-1} as the BCT composition increased from $x = 0.30$ to 0.60 in BZT-xBCT ceramics. Xiao et al. [74] also found a Raman active mode at 184 cm^{-1} in nanocrystalline BT ceramics, which was present in rhombohedral and orthorhombic phases. Hermet et al. [71] reported that the Raman active mode at $\sim$205 cm^{-1} belongs to $E(TO)$ symmetry of the rhombohedral phase of pure BT. Hence, the presence of the Raman mode at $\sim$189 cm^{-1} in this paper is attributed to the $E(TO)$ symmetry vibration, and the existence of the $E(2TO)$ mode is an indication of a rhombohedral phase of BZT-xBCT ($x = 0.30$) ceramics. The rhombohedral phase with $R3m$ symmetry of BZT-xBCT ($x = 0.30$) ceramics is also confirmed by the Rietveld refinement of the XRD spectrum. It is significant that the $A_1(1TO)$ mode slightly softens and completely disappears above $x = 0.45$, as shown in Figs. 3(a) and 3(b). The vanishing of the $A_1(1TO)$ mode and persisting of the $E(2TO)$ mode indicate the structural change in the material from rhombohedral to orthorhombic phase. In pure BT, the formation of peaks $\sim$117 and 261 cm^{-1} correspond to phonon vibrations of Ti-O bonds, whereas formation of peaks $\sim$515 and 717 cm^{-1} correspond to phonon vibrations of the Ba-O bonds. Thus, the frequency shifts of the $A_1(1TO)$ mode toward the low-frequency region for BZT-xBCT ($0.30 \leqslant x \leqslant 0.45$) may be due to dissimilar ions in the central octahedron of the perovskite structure. The BZT-xBCT ceramic with $x = 0.30$ (higher Zr content) compared with $x = 0.40$ and 0.45 experiences a downshift of the $A_1(1TO)$ frequency, which can be attributed to the variation of effective mass of the vibrational mode, as Ti is smaller than Zr. Thus, the slight softening of the $A_1(1TO)$ mode corresponds to replacement of the Zr site with Ti. These results are like those observed previously in BZT-xBCT ($0.10 \leqslant x \leqslant 0.20$) ceramics [22]. Note that the $E(2TO)$ mode stiffens with increasing the BCT compositions and completely vanishes, while the $A_1(1LO)$ mode shows a clear anomaly above $x = 0.60$, as shown in Fig. 3(d). Moreover, a new $E(2LO)$ mode appears at $\sim$466 cm^{-1} in the BZT-xBCT ($x = 0.70$) ceramic [Fig. 3(c), lower part]. The disappearance and appearance of Raman modes is a clear indication of structural transformation from orthorhombic to tetragonal phase above $x = 0.60$. It is worth noting that the $A_1(1TO)$ mode splits in the tetragonal phase but not in the rhombohedral phase [Fig. 3(b)]. This may be due to the shift of polarization from
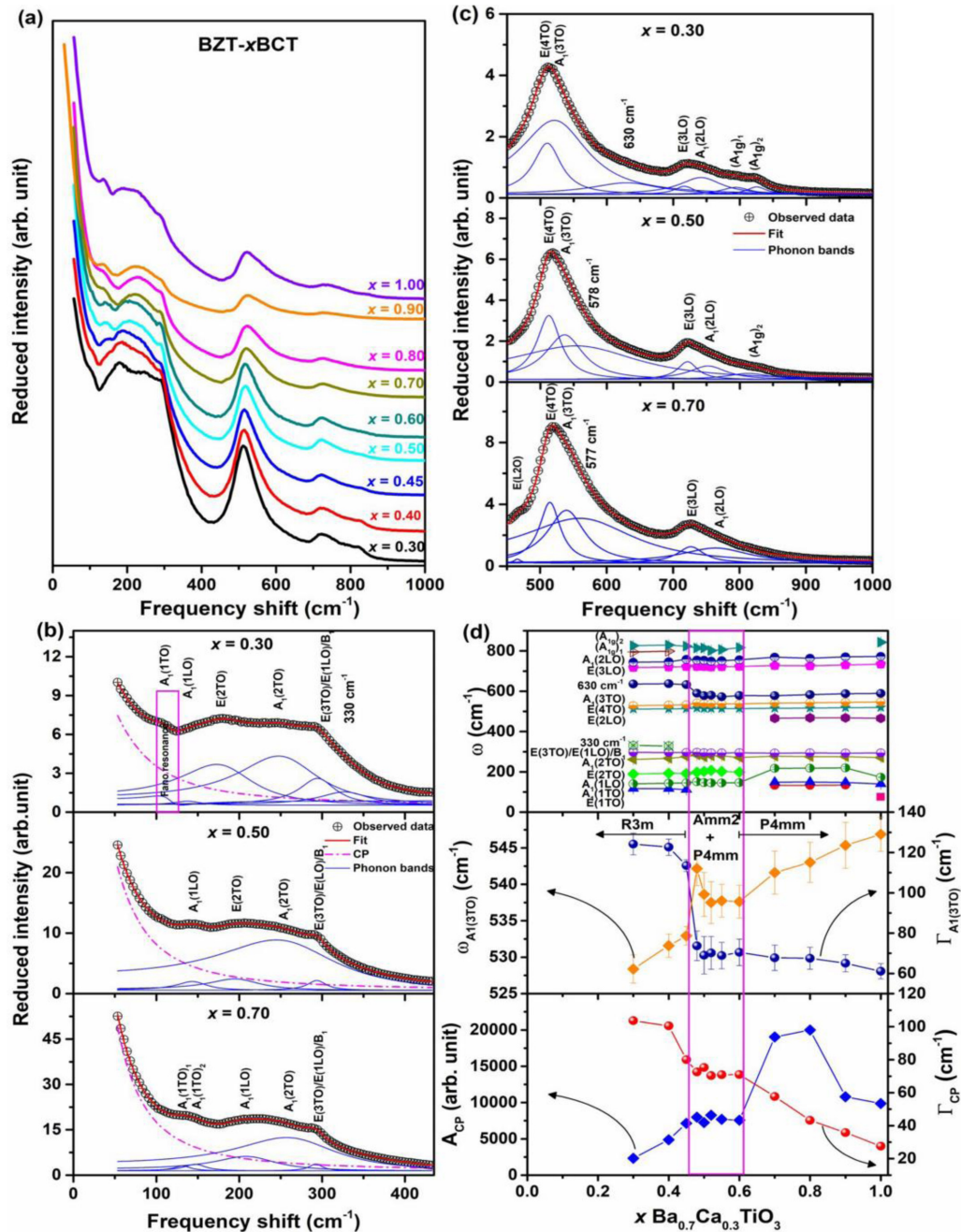
FIG. 3. (a) The composition-dependent Raman spectra of BZT-*x*BCT ceramics, (b) and (c) Raman fitted spectra using Eq. (2), and (d) the frequency shift of Raman active modes (upper part), the frequency and full width at half maximum (FWHM) of the A_1(3TO) mode (middle part), and the intensity and FWHM of the central peak (CP; lower part) of BZT-*x*BCT ceramics as a function of composition.

the [111] direction to the [001] direction through the [101] direction [75]. The Rietveld refinement of the XRD spectra of BZT-*x*BCT ($0.60 \leqslant x \leqslant 1.0$) reveals the tetragonal phase with *P4mm* symmetry, while BZT-*x*BCT ($0.45 \leqslant x \leqslant 0.55$) shows the coexistence of orthorhombic (*Amm*2) and tetragonal (*P4mm*) phases. Singh *et al.* [76] reported the coexistence of phases in BZT-*x*BCT ($x = 0.50$) by observing the hysteresis behavior of the A_1(3TO) mode. Therefore, we have also studied the A_1(3TO) mode as a function of composition to have a better understanding of the phase transitions of BZT-*x*BCT ceramics. The composition-dependent frequency and FWHM of the A_1(3TO) mode is shown in the middle part

of Fig. 3(d). It is apparent that the FWHM of the A_1(3TO) mode decreases, while the frequency shows significant stiffening and a discontinuity at above $x = 0.45$, reflecting the structural transformation from the rhombohedral phase. Note that the frequency and FWHM of the A_1(3TO) mode are almost constant in the range of $0.45 < x \leqslant 0.60$. The frequency increases and FWHM decreases continuously with increasing BCT compositions above $x = 0.60$. The constant frequency and damping of the A_1(3TO) may be due to the coexistence of phases in the range of $0.45 < x \leqslant 0.60$. Hence, the anomalous change of the A_1(3TO) mode at $x = 0.45$ corresponds to structural transformation from pure rhombohedral to orthorhombic

+ tetragonal phase, and another anomaly at $x = 0.60$ corresponds to orthorhombic + tetragonal to a pure tetragonal phase transition of BZT-xBCT ceramics. Since the formation of peaks ~515 cm^{-1} correspond to phonon vibrations of the Ba-O bonds, so the stiffening of the A_1(3TO) is likely due to replacement of the Ba site with Ca, as the atomic number of Ba is higher than that of Ca. The high-frequency region ~825 cm^{-1} shows an A_{1g} octahedral breathing mode. The symmetric A_{1g} octahedral breathing mode occurs in this region for simple perovskites and is Raman inactive and does not result in a change in polarization [77]. The A_{1g} mode [upper part of Fig. 3(c)] becomes Raman active when dissimilar ions in the center of the octahedra create asymmetry in the breathinglike mode [22]. The breathing $(A_{1g})_1$ mode merges into the $(A_{1g})_2$ mode at $x = 0.45$, and the breathing $(A_{1g})_2$ mode completely vanishes above $x = 0.60$, as shown in the upper part of Fig. 3(d). The merging and disappearing A_{1g} modes can be an indication of structural transformation as well.

In BZT-xBCT ($x = 0.30$) ceramics, the Raman spectrum is fitted using the Fano function at ~117 cm^{-1}, as shown in Fig. 3(b). The Fano resonance phenomenon stems from the interaction between a discrete state and continuum states and has an asymmetry of the spectral line shape [78]. However, the physical origin of the Fano resonance in BZT-xBCT at ~117 cm^{-1} remains unclear. The Fano resonance ~175 cm^{-1} in pure BT single crystal was attributed to the interference effect ensuing from the coupling between two acoustical phonon states and a single phonon state through the anharmonic terms in the potential function studied by Rousseau and Porto [79]. The Fano-like interference ~175 cm^{-1} in pure BT crystals may be due to the anharmonic coupling of the lowest frequency TO phonon with the higher frequency TO phonon via acoustic phonons reported by Pinczuk *et al.* [80] as well. In BZT-xBCT, the acoustic phonon mode is not observed in this paper. Hence, the coupling between the A_1(1TO) mode and acoustic phonon modes cannot be the origin of the Fano resonance in BZT-xBCT ceramics. The possible origin of the Fano resonance in BZT-xBCT at ~117 cm^{-1} may be due to the coupling between A_1(1TO) and A_1(2TO) modes [22]. Due to the vanishing of the A_1(1TO) mode, the Fano resonance also disappears in BZT-xBCT at above $x = 0.45$, as shown in Figs. 3(a) and 3(b). However, the Fano-like asymmetric line shape appears in BZT-xBCT ($x = 1.0$, BCT) near the A_1(1TO) mode [Fig. 3(a)]. In BCT, we failed to fit the Raman spectrum assuming the Fano function at ~140 cm^{-1} [A_1(1TO) mode], while the spectrum was well fitted considering the Fano function at ~173 cm^{-1} [A_1(1LO) mode] in this paper (see Fig. S2 in the Supplemental Material [13]), and this fact rules out the coupling between A_1(1TO) and A_1(2TO). It is found that the Fano resonance ~117 cm^{-1} of the BZT-xBCT ($x = 0.3$) is well fitted with a negative value of $q \sim -0.978 \pm 0.24$, and the Fano resonance ~173 cm^{-1} of the BCT is fitted with the positive value of $q \sim 1.759 \pm 0.22$. The physical origin of the Fano resonance in Li-doped KTa$_{1-x}$Nb$_x$O$_3$ single crystal at ~196 cm^{-1} has been attributed to the coupling between the broad CP, which gives rise to polarization fluctuations of local polar clusters called PNRs, and the E(2TO) mode by observing the positive q value [66,67]. The prominent CP of BZT-xBCT ($x = 1.0$) ceramics has been observed, as shown in Figs. 3(a) and 3(b). By Brillouin scattering, Ko

et al. [81] reported the CP of pure BT, which was attributed to PNRs due to off-center displacements of Ti at the B site with hopping motion along equivalent [111] directions [82]. Banerjee *et al.* [83] also studied the Fano resonance with the polarization fluctuations in PNR continua and observed a positive value of q. Thus, coupling between the broad CP and the A_1(1LO) mode may be the origin of the Fano resonance of the BCT ceramic. Recently, Pradhan *et al.* [84] reported the physical origin of the Fano resonance of Co-doped BT is the coupling between a discrete A_1(LO$_1$) phonon ~173 cm^{-1} and the broad CP, due to rapid polarization fluctuations in PNRs.

We have studied the composition dependence of the CP behavior to have a better understanding of the effects of BCT composition on local heterogeneities in BZT-xBCT ceramics. The soft mode expresses a common property of either a ceramic or a crystal undergoing the displacive phase transition, and the CP is the general property of the order-disorder phase transition of ferroelectric materials. We do not observe the low-frequency E(1TO) phonon mode in the BZT-xBCT ($0.30 \leqslant x \leqslant 0.9$) in this paper. However, we observed a phonon mode at 74 cm^{-1} [E(1TO)] in BZT-xBCT ($x = 1.0$), as shown in the Supplemental Material [13]. The E(1TO) mode was also found in the tetragonal phase of pure BT [68]. Due to lack of temperature-dependent Raman scattering results, it is difficult to comment on the soft-mode behavior of the E(1TO) mode. Therefore, the existence of prominent CP is a clear indication of the order-disorder nature of ferroelectric phase transition of BZT-xBCT ceramics [66,67,81]. It is well known that the fluctuating PNRs begin to appear at the so-called Burns temperature (T_B) in the paraelectric cubic phase [85], whereas these dynamic PNRs become static at an intermediate temperature (T^*) [66,67]. Owing to the freezing of local polarization, these static PNRs become randomly oriented nanodomain states and transform into macrodomain states in the ferroelectric phase [49,86]. It is seen from the lower part of Fig. 3(d) that the FWHM of the CP, which is related to the relaxation process of precursor dynamics [66,67,81], decreases with increasing BCT composition of BZT-xBCT ceramics. This result suggests that the correlation among nanodomain states may be strengthened with increasing BCT composition below and above the MPB region ($0.45 < x \leqslant 0.60$) due to the increase of size and/or number density of randomly oriented nanodomain states. This enhances the relaxation process of domain wall motion and results in an increase of the CP intensity. However, the intensity and FWHM of the CP is almost constant in the MPB region, in which BZT-xBCT belongs to orthorhombic + tetragonal phases. Owing to the coexistence of phases, the correlation among nanodomain states may weaken and/or be broken, giving rise to the almost constant fluctuations of domain wall motion and results in constant CP intensity in the MPB. The motion of ferroelectric domain walls of BaTiO$_3$ was observed by confocal Raman spectroscopy as well [87].

C. Theoretical results

To further elucidate the atomistic origins of the observed phase competition and functional properties of lead-free BZT-xBCT ceramics as a function of composition, we performed first-principles calculations based on DFT.
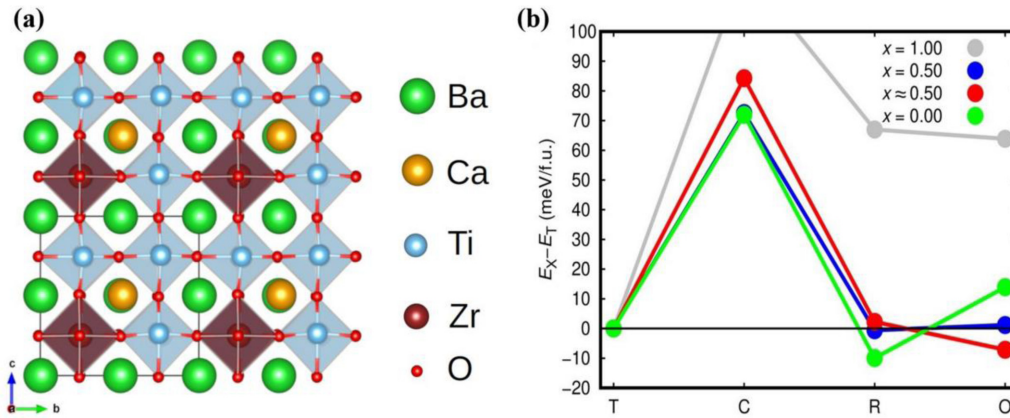
FIG. 4. First-principles characterization of lead-free BZT-xBCT ceramics based on density functional theory calculations. (a) Sketch of the simulation cell employed in the first-principles calculations (black solid lines). (b) Energy difference results as obtained for the tetragonal ($P4mm$, T), cubic ($Pm\bar{3}m$, C), orthorhombic ($Amm2$, O), and rhombohedral ($R3m$, R) phases of lead-free BZT-BCT ceramics as a function of composition.

Figure 4(a) illustrates the unit cell, and Fig. 4(b) shows the zero-temperature DFT energy estimated for the four selected BZT-xBCT polymorphs (i.e., tetragonal $P4mm$, cubic $Pm\bar{3}m$, rhombohedral $R3m$, and orthorhombic $Amm2$) considering four different compositions.

In accordance with the experiments, we find a very strong phase competition between the three polar tetragonal, rhombohedral, and orthorhombic polymorphs for compositions around $x = 0.50$ (the two simulated composition systems $x = 1.00$ and 0.00 also reproduce the stable phases observed in the XRD and Raman experiments [Fig. 4(b)].

Specifically, at $x = 0.50$, the energy differences between the three polar phases are of the order of 1 meV/f.u. or below, and we predict the rhombohedral phase to be the ground-state structure (note that thermal effects are systematically disregarded in our first-principles calculations). As the content of BCT is marginally reduced, the orthorhombic polymorph clearly becomes energetically more favorable than the others. For instance, at $x \approx 0.50$, the energy difference between the orthorhombic and tetragonal polymorphs is 7 meV/f.u. and between the orthorhombic and rhombohedral is 9 meV/f.u. Thus, the DFT calculations are in good agreement with the observation that, upon varying the ceramics composition from $x = 0.50$ to 0.45, the fraction of the orthorhombic phase increases considerably.

D. Surface morphology

Figures S3(a)–S3(c) in the Supplemental Material [13] show SEM of BZT-xBCT for $x = 0.4$, 0.5, and 0.6 as representative images (other compositions are not shown here). The micrographs show highly dense microstructure in which the polyhedral grains are well developed and separated by grain boundaries. The grains are inhomogeneously distributed throughout the microstructure with a few scattered pores. The surface microstructure of BZT-xBCT samples is strongly dependent on the composition. The average grain size was calculated using IMAGEJ software. The grain size of $x = 0.3$ is found to be 1.5 μm with very fine and well-connected grains. The grain size increases with an increase in BCT

concentration, and for pure BCT, the grain size is found to be ~13 μm, as shown in the Fig. S3(d) in the Supplemental Material [13]. This implies that BCT promotes the grain growth of the material. The elemental composition in our system was further investigated via EDX. EDX spectra show the presence of all the cationic elements in the compounds with proper stoichiometry within an error limit of $\pm10\%$ (provided in Fig. S4 in the Supplemental Material [13]).

E. Electrical properties

1. Dielectric properties

To study the phase transition behavior in BZT-xBCT ceramics, temperature-dependent dielectric properties, i.e., dielectric permittivity (ε_r) and dielectric loss (tanδ) for different frequencies, were investigated. The temperature-dependent dielectric permittivity and dielectric loss at various frequencies for BZT-xBCT with $x = 1.0$, 0.55, 0.5, and 0.4 are shown in Figs. 5(a)–5(d) as representative plots. The dielectric permittivity decreases with increasing frequency for all compositions irrespective of temperature, suggesting the typical behavior of polar dielectric materials, as shown in Fig. 5. For all compositions, the dielectric permittivity increases with increase in temperature at all frequencies up to the ferroelectric phase transition temperature. With further increase in temperature, the dielectric permittivity values decrease. For pure BCT ($x = 1.0$), the ferroelectric-to-paraelectric phase transition is a sharp phase transition with a transition temperature of 120 °C, as observed in Fig. 5(a). With decreasing BCT concentration, the phase transition becomes more diffuse, i.e., broadening of the phase transition around T_m. For $x = 0.3$ and 0.4, a highly diffuse phase-transition behavior is observed. This result is consistent with previous reports of the PMN-PT system [88]. Similarly, from the dielectric loss plots, a single sharp anomaly is observed for pure BCT, and the peak becomes broadened at higher BZT concentrations. Diffuse phase transitions in a material are generally characterized by certain features such as (i) the broadness of dielectric permittivity (ε_r) vs temperature curve, (ii) a relatively large difference in the temperature corresponding to the maximum dielectric
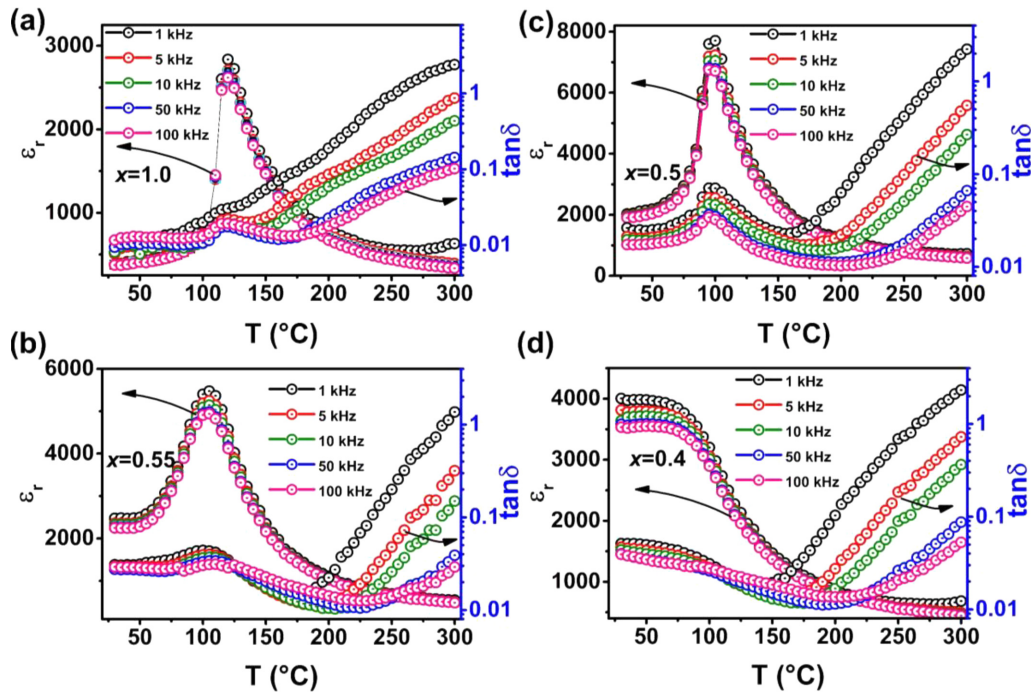
FIG. 5. Temperature (T) dependence of dielectric permittivity, and dielectric loss of BZT-xBCT with the composition (a) $x = 1.0$, (b) $x = 0.55$, (c) $x = 0.5$, and (d) $x = 0.4$ at some selected frequency.

permittivity (ε_r) and dielectric loss (tanδ) of the dielectric spectra, (iii) frequency dispersion of both ε_r and tanδ in the transition region, suggesting a frequency-dependent temperature of maximum dielectric permittivity, and (iv) a deviation from the Curie-Weiss law in the vicinity of maximum dielectric temperature [89].

The broad dielectric curve at higher BZT content is due to the larger ionic radius and lower polarization value of Zr^{4+} than Ti^{4+} [27]. The observed diffuse phase transition is due to the cation disorder, i.e., compositional fluctuation of the different polar microregions where different ions (Ba^{2+}, Ca^{2+}, Ti^{4+}, and Zr^{4+}) occupy the same crystallographic sites in the ABO_3 perovskite.

Further, to quantify the diffuseness, the modified Curie-Weiss equation is used to fit the temperature-dependent dielectric permittivity data. The modified Curie-Weiss equation can be expressed as $(1/\varepsilon_r) - (1/\varepsilon_m) = [(T - T_m)^{\Upsilon}]/C$, where $C = 2\varepsilon_m \delta^{\Upsilon}$, ε_m is the dielectric permittivity at T_m, T_m represents the temperature at which maximum dielectric permittivity is observed, γ the degree of relaxation/diffuseness, δ the diffuseness parameter, and C the Curie-Weiss constant. The value of γ is found to be 1 for normal ferroelectric and $\sim$2 for highly diffuse ferroelectric phase transitions [90]. To verify the modified Curie-Weiss law, the temperature-dependent dielectric permittivity data have been plotted in a log-log plot in the paraelectric region (just above the T_m), as shown in the inset Fig. 6(c) for $x = 0.5$. The linear fit of this plot suggests the verification of the modified Curie-Weiss equation. The slope of the curve gives the value of γ, and from the intercept of this curve, δ can be calculated.

For all compositions, the values of γ and δ are plotted as a function of composition, as shown in Fig. 7. The γ value is found to be 1.1 for pure BCT; however, with decreasing BCT

concentration, this value increases to 1.8 for $x = 0.4$ (shown in Fig. 7). There is a discontinuous change in the γ value with the composition around the phase coexistence region. This confirms the material exhibits a strong diffuse phase transition at higher BZT concentration [89]. For $x = 0.5$, the fitted parameters are found to be $\gamma = 1.47$ and $\delta = 23.6$, which is close to the previously reported value [34]. The ferroelectric transition temperature T_m and ε_m (around T_m) are strongly dependent on the composition, as shown in Fig. 7. It is observed that ε_m increases with the increasing BCT composition up to $x = 0.5$; increasing BCT beyond $x = 0.5$, ε_m decreases. Such a large dielectric response at $x = 0.5$ is coincident with the MPB ($Amm2 + P4mm$) region. The observed phase-transition temperatures match well with previously reported values [91]. We have also calculated the tolerance factor (t) for the entire composition range. The tolerance factor decreases with increasing BCT concentrations, where the higher transition temperature correlates with lower tolerance factors, as predicted by Eitel *et al.* [92].

a. Evidence of relaxor ferroelectricity. Figure 6(a) depicts the temperature-dependent dielectric permittivity and loss tangent data for BZT-xBCT ($x = 0.5$) at different frequencies in the temperature range of 50–150 °C. Similarly, the temperature-dependent dielectric properties are also observed for compositions $x = 0.45$, 0.48, 0.52, and 0.55 (shown in Figs. S5–S8 in the Supplemental Material [13]). A single broad dielectric anomaly in the temperature-dependent dielectric permittivity is observed $\sim$100 °C (T_m) for $x = 0.5$. The dispersion in the dielectric permittivity is more pronounced around T_m. However, with the increasing temperature, the degree of dispersion decreases and vanishes $>$190 °C. This type of behavior suggests the formation of PNRs, which is a typical characteristic of relaxor ferroelectricity [34,93]. The
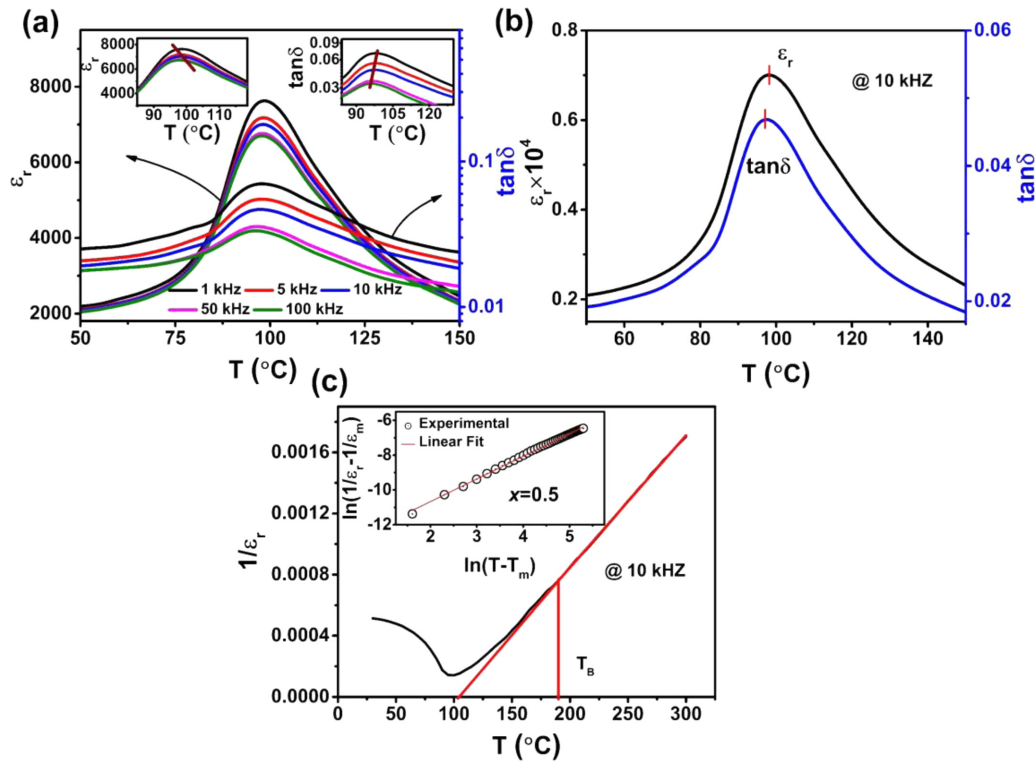
FIG. 6. (a) Temperature (T) dependence of dielectric permittivity and dielectric loss at different frequencies for the composition $x = 0.5$. The inset of (a) shows the magnified plot of temperature-dependent dielectric permittivity and dielectric loss to reveal the frequency dependence of the peak temperature. (b) Magnified plot of dielectric permittivity and dielectric loss to reveal the difference in the corresponding peak temperature at a given frequency of 10 kHz for $x = 0.5$. (c) Variation of $1/\varepsilon_r$ as a function of temperature at 10 kHz with $x = 0.5$; T_B corresponds to Burn temperature. Inset of (c) shows a modified Curie-Weiss law fit [$\ln(1/\varepsilon_r - 1/\varepsilon_m)$ vs $\ln(T - T_m)$] of temperature-dependent dielectric permittivity.

dielectric permittivity peak slightly shifts toward higher temperature with increasing frequency around T_m, which is clearly visible in the inset of Fig. 6(a). On the other hand, the opposite trend is observed for the loss tangent, i.e., upon increasing frequency, the loss peak shifts toward lower temperatures [as observed in the inset of Fig. 6(a)]. To further illustrate this point, we have plotted the dielectric permittivity and loss at a frequency of 10 kHz around the phase-transition region, as shown in Fig. 6(b). There is a small difference in the transition temperature for the permittivity and loss peak, i.e., the dielectric permittivity peak occurs at a higher temperature relative to the loss peak [34,93]. This type of behavior confirms the relaxor nature of the analyzed material, and our observation is consistent with a previous report [34]. A similar type of behavior is also observed for other MPB compositions, i.e., $x = 0.45$, 0.48, 0.52, and 0.55 (see Figs. S5–S8 in the Supplemental Material [13]).

The temperature below which the frequency-dependent dielectric permittivity curve branches off can be considered the Burns temperature (T_B). Furthermore, the temperature around which the deviation from the Curie-Weiss behavior is observed can be regarded as T_B, as it has been previously justified in the literature [34]. The plot of $1/\varepsilon_r$ expressed as a function of temperature at 10 kHz is shown in Fig. 6(c) and used to determine T_B. A significant departure from the Curie-Weiss behavior is observed below 190 °C, suggesting this temperature to be T_B (below which the dynamic polar

regions are expected to appear) [64,94]. Upon cooling, the PNRs start to develop inside the crystal instead of micrometer scale ferroelectric domains with randomly oriented dipole moments. Note that T_B is well above T_m [95]. These PNRs are not static in nature at T_B, with the dipole moment thermally fluctuating between equivalent polarization directions [96]. All of the above points to the relaxor behavior for the composition $x = 0.5$. This type of relaxor behavior is present mainly for $x = 0.48$ and 0.52 in the MPB compositions. However, around T_m, a broad dielectric peak and weak dispersion behavior is observed for the MPB compositions at $x = 0.45$ and 0.55, but ε_r and tanδ peaks occur at nearly the same temperature. This suggests a weak relaxorlike behavior for these compositions (see Figs. S5–S8 in the Supplemental Material [13]). In the rhombohedral phase, the phase transition is more diffusive, and in the tetragonal phase region, the phase transition is sharp. However, around the MPB compositions, weak relaxorlike behavior is clearly visible.

2. Ferroelectric properties

To confirm the ferroelectric behavior, room-temperature ferroelectric (P-E) hysteresis loops for BZT-xBCT were recorded in the composition range of $0.3 \leqslant x \leqslant 1.0$. Figures 8(a)–8(c) show the hysteresis loop of poled samples at a testing frequency of 10 Hz. The shape of the P-E loop changes with changing BZT-xBCT compositions, as shown in the
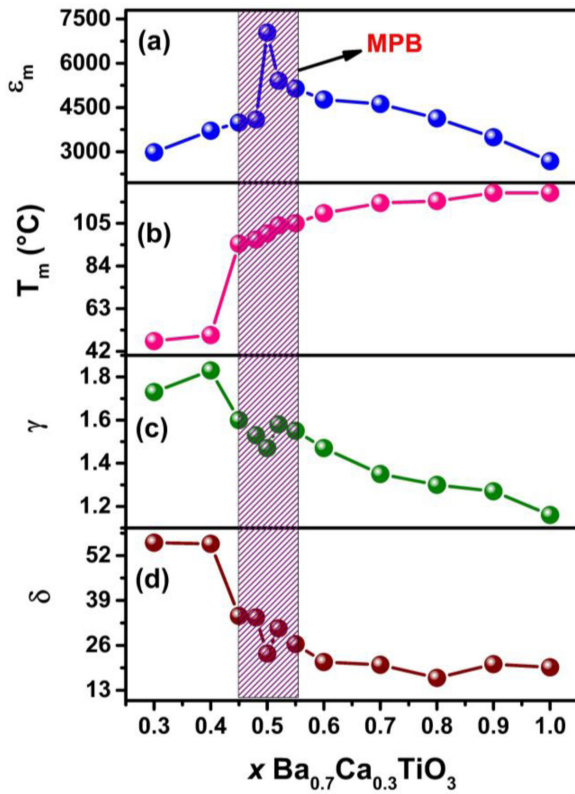
FIG. 7. Variation of (a) dielectric permittivity (ε_m) around transition temperature (T_m). (b) Transition temperature (T_m). (c) Degree of diffuseness (γ). (d) Diffuseness parameter (δ) with composition (x) of BZT-xBCT in the composition range of $0.3 \leqslant x \leqslant 1.0$.

Figs. 8(a)–8(c). Higher BZT concentrations ($x = 0.3-0.4$) exhibit a narrow hysteresis loop, suggesting the samples are soft in nature with respect to applied electric field [97,98]. This narrow *P-E* loop can be attributed to the combination of macro- and micropolar regions and results in an enhanced diffused phase transition effect [99]. This behavior is consistent with the temperature-dependent dielectric results. However, with increasing BCT concentration, the area of the hysteresis loop increases, which implies more energy required to reverse the dipole. The *P-E* loop exhibits a nonlinear, well-defined, and saturated loop for all the compositions. The ferroelectric parameters such as remnant polarization $2P_r = P_r^{+0} - P_r^{-0}$ and coercive field $E_c = (E_c^{+0} - E_c^{-0})/2$ are calculated from the *P-E* loops. The switchable polarization, i.e., $2P_r$, and the coercive field (E_c) are plotted as a function of x in Fig. 8(d). The composition $x = 0.3$ exhibits a low remnant polarization ($2P_r$) value of 5.38 μC/cm^2 with a low coercive field of 1.59 kV/cm. The $2P_r$ increases with increasing BCT concentration, and the maximum value is found to be 19.47 μC/cm^2 for $x = 0.5$.

At higher BCT composition, $2P_r$ value decreases up to $x = 1.0$. The rate of increasing/decreasing polarization value is greatest in the phase coexistence regions, i.e., around MPB compositions. However, the coercive field (E_c) increases with increasing BCT concentrations up to $x = 0.6$ and above this composition, the E_c value saturates. The value of coercive field for the rhombohedral phase ($x = 0.3$ and 0.4) is much

lower than the value of the tetragonal phase ($0.6 \leqslant x \leqslant 1.0$), which is consistent with a previous report [100]. The lower values of both $2P_r$ and E_c in the rhombohedral ($0.3 \leqslant x \leqslant 0.4$) phase imply a disturbance of the long-range ferroelectric ordering due to the restriction in ionic displacement (decrease in the rattling space available for the movement of B-site cations) because of the higher ionic radii of Zr^{4+} than Ti^{4+} [97]. The lower values of both $2P_r$ and E_c can also be due to the uniform grain size and decrease in the tetragonal phase fraction, which is consistent with both XRD and microscopy results. The lower value of $2P_r$ in the tetragonal phase region is due the decrease in the unit cell volume with increasing BCT concentration. The higher E_c value in the tetragonal phase suggests the domain wall pinning phenomena. The higher value of $2P_r$ with a low value of coercive field, as observed in the range of $0.45 \leqslant x \leqslant 0.55$, is consistent with a MPB region [shown in Fig. 8(d)], as shown in previous theoretical reports [10–12].

3. Piezoelectric properties

The variation of the piezoelectric coefficient (d_{33}) of BZT-xBCT ceramics as a function of BCT concentration at room temperature is shown in Fig. 9. The d_{33} value is found to be 29 pC/N for $x = 0.3$. With increasing BCT content, the d_{33} value increases and reaches to a maximum value for $x = 0.5$, then decreases with a further increase in BCT concentration. The rate of change in the d_{33} value is higher in the composition range of $0.45 \leqslant x \leqslant 0.55$ (in the phase coexistence MPB region) with the maximum value of d_{33} found to be 320 pC/N for $x = 0.5$. The variation of d_{33} is like the variation of ε_r and P_r with composition, and the maximum value of these physical properties all correlate to the $x = 0.5$ composition. The reason for the enhancement of d_{33} around the MPB is discussed below.

IV. DISCUSSION

The observation of the composition-driven structural phase transition around the MPB region of perovskite-based solid solutions is of great practical interest as well from the fundamental physics point of view [101]. The origin of the MPB composition in ferroelectric solid solutions has been studied based on the Landau free energy functions, and it has been reported that the composition in the vicinity of MPB region shows large dielectric susceptibility and piezoelectric coefficients with extremely small coercive field and stiffness constant [10–12]. First-principles and phenomenological investigations suggest that the anisotropic flattening of the free energy profile gives rise to the polarization rotation with a low-energy pathway around the MPB compositions and thus the principal mechanism for the enhanced piezoelectric properties [102,103]. The piezoelectric coefficient d of the ferroelectric oxides having a perovskite structure can be represented by $d = 2P_S Q\varepsilon$, where P_S = spontaneous polarization, Q = the electrostrictive coefficient, and ε = dielectric permittivity [102,104]. Using the phenomenological thermodynamic theory, the dielectric permittivity [i.e., dielectric susceptibility (χ) $\sim$ dielectric permittivity for ferroelectric systems] is represented by the curvature of the free energy density profile with respect to polarization (i.e., $\partial^2 G/\partial p^2 \propto 1/\chi$)
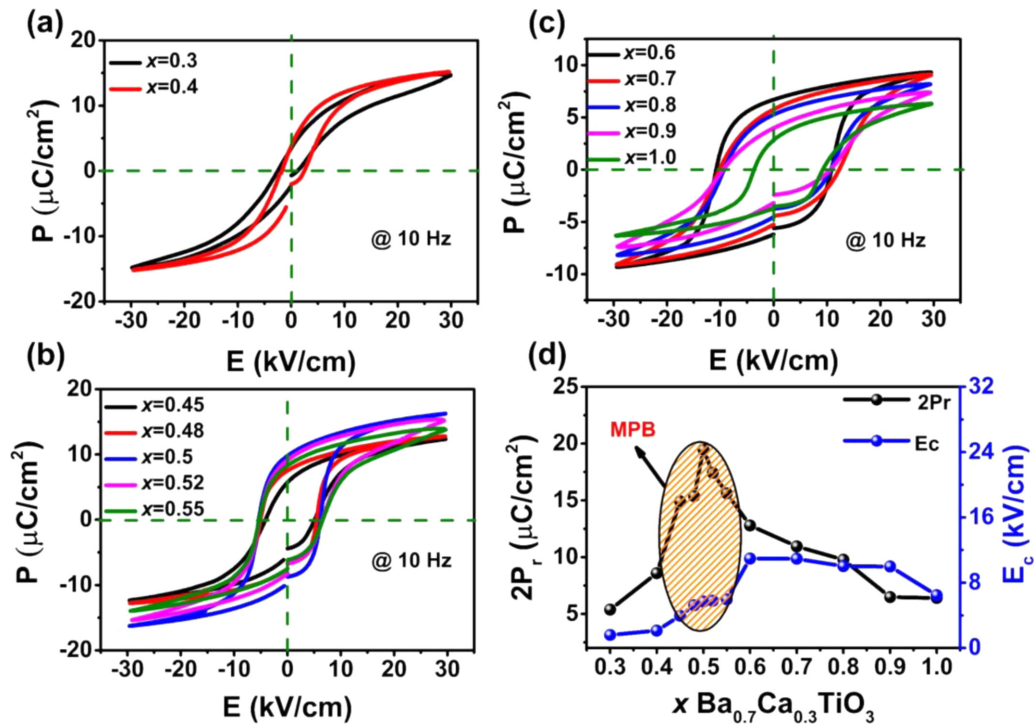
FIG. 8. Ferroelectric hysteresis (P-E) loop of poled sample of BZT-xBCT ceramic for (a) $x = 0.3 - 0.4$, (b) $x = 0.45 - 0.55$, and (c) $x = 0.6 - 1.0$. (d) Variation of $2P_r$, E_c for BZT-xBCT with the composition range of $0.3 \leqslant x \leqslant 1.0$.

[7,53,102,104]. Small curvature, i.e., a flat free energy profile, produces a higher value of ε, which is ultimately responsible for the enhancement of the piezoelectric coefficient. It has been well accepted that the free energy profile flattens around MPB compositions of the ferroelectric solid solutions, which is responsible for the enhancement of ε as well as d. As the composition-induced structural phase transition is a first-order phase transition (this signature has been reflected in terms of the coexistence of tetragonal and orthorhombic crystallographic phases in our case), an ideally flat free energy profile

FIG. 9. Variation of d_{33} for BZT-xBCT within the composition range of $0.3 \leqslant x \leqslant 1.0$.

(i.e., $\partial^2 G / \partial p^2$ tends to zero) cannot be achieved. However, the free energy profile can further flatten by inducing a local structural heterogeneity to manipulate the interfacial energy, i.e., electrostatic and elastic energy associated with the interface [103,104]. Based on computational and experimental investigations, Acosta *et al.* [52] suggested that the enhanced piezoelectric properties in the BZT-xBCT system around the MPB region cannot be fully reconciled by the reduction in the anisotropic energy or flattening of the free energy. They further suggest that the reduction of the anisotropic energy is the necessary condition for enhanced piezoelectric properties but not the sufficient condition for maximizing the piezoelectric properties, which was further supported by Cordero *et al.* [52,105]. The optimum/sufficient condition is the greatest elastic softening and retention of high spontaneous/remnant polarization [105].
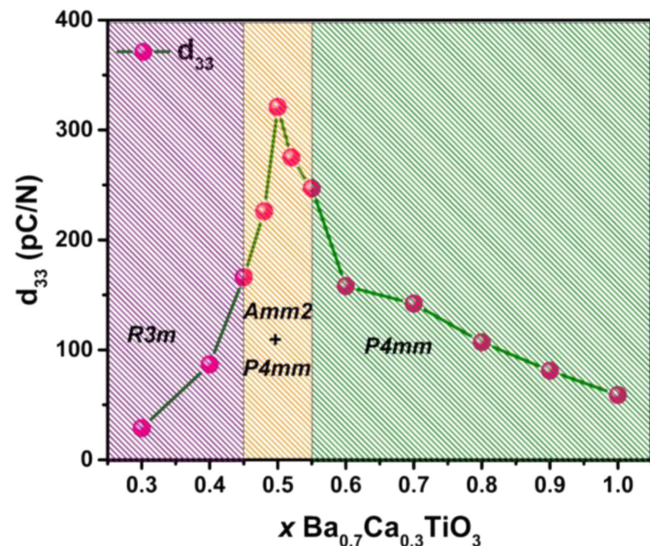
The symmetry-allowed polarization rotation phenomena can be used to explain the enhancement of the piezoelectric properties due to flattening of anisotropic free energy in the BZT-xBCT system around the MPB due to composition-induced structural phase transitions [103,106]. At $x = 1.0$, BCT belongs to the tetragonal ($P4mm$) crystal structure, and $x = 0.3$ belongs to the rhombohedral ($R3m$) crystal structure. The transition from $P4mm$ to $R3m$ is not allowed by the symmetry considerations; however, it can be mediated through a low-symmetry phase [20,52,106]. The tetragonal strain is dominant over the rhombohedral strain, which induces an orthorhombic instability in the lattice and serves as a structural bridge (where polarization rotation occurs among the different polarization states) connecting $R3m$ and $P4mm$ phases in the MPB [27]. As the BT-based system is like the PZN $-$ xPT system, the low-symmetry orthorhom-

bic (*Amm*2) phase can be expected [103]. The BZT-*x*BCT system undergoes a phase transition from the rhombohedral (*R*3*m*) to tetragonal (*P*4*mm*) phase through the coexistence of tetragonal (*P*4*mm*) + orthorhombic (*Amm*2) phases in the MPB region, as confirmed from the XRD and Raman data. The polarization vector rotates from the rhombohedral [111] direction (*R*3*m*) to the tetragonal [001] direction (*P*4*mm*) through the [101] orthorhombic direction (*Amm*2). The polarization rotation behavior has been described in Fig. S9 in the Supplemental Material [13]; also see Refs. [107–110] therein. The orthorhombic phase (*Amm*2) is the intermediate phase between the rhombohedral (*R*3*m*) and tetragonal (*P*4*mm*) phases; thus, the polarization rotation mechanism is applicable for the MPB composition of this BZT-*x*BCT ferroelectric solid solution [103].

From the first-principles DFT calculations, we have observed a strong phase competition around the MPB, and the orthorhombic phase is stabilized as the ground state for a narrow composition range like the previous path integral Monte Carlo quantum mechanical simulation result [53]. The local structure in the orthorhombic (*Amm*2) phase is expected to be more disordered/fragmented than that of BT and allows easier fluctuations of the polarization BZT-*x*BCT system around MPB [53]. The prominent CP can be evidence of the existence of local polar structure in BZT-*x*BCT by Raman scattering. Thus, the presence of the orthorhombic (*Amm*2) phase induces large fluctuations of the polarization, which gives rise to the low-energy barrier between the *Amm*2 and *P*4*mm* ferroelectric phases (the energy difference between *Amm*2 and *P*4*mm* phases is 7 meV/f.u., as observed from DFT calculations), leading to easy polarization rotations. In short, the easy polarization rotation is responsible for high piezoelectric properties around the MPB region, which may be the necessary condition as proposed by Acosta *et al.* [52].

The extrinsic contribution of domain switching can also further flatten the polarization anisotropy energy [54]. It is well established that ferroelectric materials belonging to either a tetragonal or rhombohedral crystal structure can have pinned domains; however, for the coexistence phases, the domains do switch [111]. The coexistence of *Amm*2 + *P*4*mm* phases show significant domain switching with limited intergranular constraints and manifest significant strain. The domain wall motions between different phases of different symmetry (*Amm*2 + *P*4*mm* phases in the present case) further reduces the free energy barrier to interface tension and strengthen the electromechanical response [111]. The question then arises: why the functional properties are maximum for $x = 0.5$?

From the XRD data, we have observed the discontinuity in the cell parameters and unit cell volume (around $x = 0.5$) representing first-order phase transitions, which indicate the critical point where the piezoelectric coefficient is maximum [112]. Pramanic *et al.* [113], based on an *in situ* XRD experiment, demonstrated that the decrease in tetragonality ($c/a - 1$) is well correlated with enhanced non-180° (ferroelectric/ferroelastic) domain wall motion, which significantly enhanced the piezoelectric properties. The decrease of tetragonality is associated with enhanced domain wall motion, which influences the piezoelectric and dielectric properties [31,113]. From XRD data, it has been observed that the tetrag-

onality decreases with increasing BZT concentrations with a minimum around $x = 0.5$. Thus, the domain wall contribution increases with decreasing the BCT concentration, and the maximum contribution of the domain wall motion is observed around $x = 0.5$, which is further responsible for the enhancement of the piezoelectric properties. The motion of domain walls in BZT-*x*BCT is also in agreement with the CP behavior observed in Raman scattering.

In the BZT-*x*BCT system, the tetragonal (i.e., BCT; $x = 1.0$) ferroelectric domains have long-range order, and the local structural heterogeneity tries to break the long-range polar order with an increase in the BZT concentration (i.e., due to the increase in Zr concentration) [49]. However, the local structural heterogeneity does not impact the long-range polarization of the ferroelectric (tetragonal) phase up to $x = 0.6$. In the MPB compositions ($0.45 \leqslant x \leqslant 0.55$), the local structural heterogeneity creates heterogeneous/PNRs, as observed by the relaxor ferroelectric nature from temperature-dependent dielectric data. The local heterogeneous PNRs favor the orthorhombic phase due to large fluctuations of their polarization within the macroscopic *Amm*2 phase. This supports a previous work, which shows the enhancement of piezoelectric properties by introducing a structural heterogeneity at the local scale [43]. Although the orthorhombic phase exists in the MPB region, at the critical composition ($x = 0.5$), the interfacial energy favors the transformation/alignment of the local PNRs along the long-range polarization of the tetragonal state, which tends to minimize the polarization discontinuity. Thus, at the critical composition, the critical interfacial energy (the interface energy such as electrostatic, elastic, and gradient energy) leads to the further flattening of the free energy profile so that the enhancement of the piezoelectric properties is observed for $x = 0.5$.

Thus, the enhancement of the piezoelectric properties for 0.5BZT-0.5BCT is due to combined and cooperative contributions such as (i) easy polarization rotation, (ii) maximum domain wall motion and critical interfacial energy due to the structural heterogeneity at the critical composition, and (iii) the emergence of PNRs due to relaxor behavior, which gives rise to very strong electromechanical coupling. Thus, the induction of the structural heterogeneity at the critical composition can be used as a guide to further improve the functional properties of the ferroelectric and multiferroic systems.

V. CONCLUSIONS

The $(1 - x)\mathrm{Ba(Zr_{0.2}Ti_{0.8})O_3}$-$x(\mathrm{Ba_{0.7}Ca_{0.3}})\mathrm{TiO_3}$ ($0.3 \leqslant x \leqslant 1.0$) samples were thoroughly invested near the MPB for their enhanced functional properties. The effect of compositions, especially near the MPB, has been studied to correlate the structure, microstructure, dielectric, ferroelectric, and piezoelectric properties. XRD and Raman spectroscopy studies indicate a structural phase transition from a single rhombohedral (*R*3*m*) phase with $x \leqslant 0.4$ to tetragonal (*P*4*mm*) phase for $x \geqslant 0.6$ through a multiphase coexistence region of (*Amm*2 + *P*4*mm*) for $0.45 \leqslant x \leqslant 0.55$. First-principles DFT calculations confirm the phase competition behavior in the coexistence region. The multiphase coexistence region with composition $x = 0.5$ shows enhanced dielectric, ferroelectric, and piezoelectric properties around the MPB region. With the

increase in BCT content, $2P_r$ and d_{33} values increase and reach maximum values for $x = 0.5$, then decrease with a further increase in the BCT concentration. The enhancement of the piezoelectric properties around the MPB can be attributed to the combined and cooperative contributions from easy polarization rotation and maximum domain wall motion due to the structural heterogeneity. The large dielectric permittivity, saturated hysteretic polarization, and d_{33} values make them suitable for the replacement of Pb-based materials and have strong potential to be utilized in information and/or energy storage and electromechanical devices.

ACKNOWLEDGMENTS

[1] B. Jaffe, W. R. Cook, and H. Jaffe, *Piezoeletric Ceramics* (Academic Press, London, 1971).

[2] K. Uchino, *Advanced Piezoelectric Materials: Science and Technology* (Woodhead Publishing, Philadelphia, PA, 2010).

[3] A. K. Kalyani, H. Krishnan, A. Sen, A. Senyshyn, and R. Ranjan, Phys. Rev. B **91**, 024101 (2015).

[4] J. Rödel, W. Jo, K. T. P. Seifert, E. M. Anton, T. Granzow, and D. Damjanovic, J. Am. Ceram. Soc. **92**, 1153 (2009).

[5] Y. S. Sung, J. M. Kim, J. H. Cho, T. K. Song, M. H. Kim, H. H. Chong, T. G. Park, D. Do, and S. S. Kim, Appl. Phys. Lett. **96**, 022901 (2010).

[6] Y. Saito, H. Takao, T. Tani, T. Nonoyama, K. Takatori, T. Homma, T. Nagaya, and M. Nakamura, Nature (London) **432**, 84 (2004).

[7] W. Liu and X. Ren, Phys. Rev. Lett. **103**, 257602 (2009).

[8] A. A. Heitmann and G. A. Rossetti, J. Am. Ceram. Soc. **97**, 1661 (2014).

[9] A. K. Kalyani, K. Brajesh, A. Senyshyn, and R. Ranjan, Appl. Phys. Lett. **104**, 252906 (2014).

[10] Y. Ishibashi and M. Iwata, Jpn. J. Appl. Phys. **37**, L985 (1998).

[11] M. Iwata, H. Orihara, and Y. Ishibashi, Jpn. J. Appl. Phys. **40**, 703 (2001).

[12] M. Iwata and Y. Ishibashi, Jpn. J. Appl. Phys. **38**, 5670 (1999).

[13] See Supplemental Material at http://link.aps.org/supplemental/10.1103/PhysRevB.104.224105 for additional details information on XRD, Raman spectroscopy, surface morphology and EDX spectra, dieletric properties, polarization rotation model, and a brief review on the crystal structure and symmetry of the BZT-xBCT system.

[14] W. Li, Z. Xu, R. Chu, P. Fu, and G. Zang, Phys. B: Condens. Matter **405**, 4513 (2010).

[15] V. S. Puli, A. Kumar, D. B. Chrisey, M. Tomozawa, J. F. Scott, and R. S. Katiyar, J. Phys. D: Appl. Phys. **44**, 395403 (2011).

[16] B. Li, J. E. Blendell, and K. J. Bowman, J. Am. Ceram. Soc. **94**, 3192 (2011).

[17] M. C. Ehmke, S. N. Ehrlich, J. E. Blendell, and K. J. Bowman, J. Appl. Phys. **111**, 124110 (2012).

[18] I. K. Jeong and J. S. Ahn, Appl. Phys. Lett. **101**, 242901 (2012).

[19] W. Li, Z. Xu, R. Chu, P. Fu, and G. Zang, Curr. Appl. Phys. **12**, 748 (2012).

[20] D. S. Keeble, F. Benabdallah, P. A. Thomas, M. Maglione, and J. Kreisel, Appl. Phys. Lett. **102**, 092903 (2013).

[21] B. Li, M. C. Ehmke, J. E. Blendell, and K. J. Bowman, J. Eur. Ceram. Soc. **33**, 3037 (2013).

[22] V. S. Puli, D. K. Pradhan, W. Pérez, and R. S. Katiyar, J. Phys. Chem. Solids **74**, 466 (2013).

[23] M. Sindhu, N. Ahlawat, S. Sanghi, R. Kumari, and A. Agarwal, J. Appl. Phys. **114**, 164106 (2013).

[24] D. Fu, Y. Kamai, N. Sakamoto, N. Wakiya, H. Suzuki, and M. Itoh, J. Phys. Condens. Matter **25**, 425901 (2013).

[25] I. Coondoo, N. Panwar, H. Amorín, M. Alguero, and A. L. Kholkin, J. Appl. Phys. **113**, 214107 (2013).

[26] A. B. Haugen, J. S. Forrester, D. Damjanovic, B. Li, K. J. Bowman, and J. L. Jones, J. Appl. Phys. **113**, 014103 (2013).

[27] Y. Tian, L. Wei, X. Chao, Z. Liu, and Z. Yang, J. Am. Ceram. Soc. **96**, 496 (2013).

[28] E. V. Ramana, A. Mahajan, M. P. F. Graça, S. K. Mendiratta, J. M. Monteiro, and M. A. Valente, Mater. Res. Bull. **48**, 4395 (2013).

[29] J. Gao, L. Zhang, D. Xue, T. Kimoto, M. Song, L. Zhong, and X. Ren, J. Appl. Phys. **115**, 054108 (2014).

[30] P. Mishra, Sonia, and P. Kumar, Ceram. Int. **40**, 14149 (2014).

[31] G. Tutuncu, B. Li, K. Bowman, and J. L. Jones, J. Appl. Phys. **115**, 144104 (2014).

[32] Z. Sun, Y. Pu, Z. Dong, Y. Hu, P. Wang, X. Liu, and Z. Wang, Mater. Sci. Eng. B **185**, 114 (2014).

[33] H. Guo, B. K. Voas, S. Zhang, C. Zhou, X. Ren, S. P. Beckman, and X. Tan, Phys. Rev. B **90**, 014103 (2014).

[34] K. Brajesh, K. Tanwar, M. Abebe, and R. Ranjan, Phys. Rev. B **92**, 224112 (2015).

[35] J. P. Praveen, T. Karthik, A. R. James, E. Chandrakala, S. Asthana, and D. Das, J. Eur. Ceram. Soc. **35**, 1785 (2015).

[36] K. Brajesh, M. Abebe, and R. Ranjan, Phys. Rev. B **94**, 104108 (2016).

[37] P. Adhikari, R. Mazumder, and S. Abhinay, J. Electroceram. **37**, 127 (2016).

[38] P. Adhikari, R. Mazumder, and G. K. Sahoo, Ferroelectrics **490**, 60 (2016).

[39] L. Zhang, X. Ren, and M. A. Carpenter, Phys. Rev. B **95**, 054116 (2017).

[40] H. Kaddoussi, A. Lahmar, Y. Gagou, B. Manoun, J. N. Chotard, J. L. Dellis, Z. Kutnjak, H. Khemakhem, B. Elouadi, and M. E. Marssi, J. Alloys Compd. **713**, 164 (2017).

[41] A. R. Montero, F. R. Marcos, L. Pardo, A. D. Campo, R. L. -Juárez, and M. E. V. Castrejón, J. Mater. Chem. A **6**, 5419 (2018).

[42] B. C. Keswani, S. I. Patil, A. R. James, Y. D. Kolekar, and C. V. Ramana, Ceram. Int. **44**, 20921 (2018).

[43] A. Akbarzadeh, K. Brajesh, Y. Nahas, N. Kumar, S. Prokhorenko, D. Swain, S. Prosandeev, R. Walter, I. Kornev, J. Íñiguez, B. Dkhil, R. Ranjan, and L. Bellaiche, Phys. Rev. B **98**, 104101 (2018).

[44] A. R. Jayakrishnan, K. V. Alex, A. Thomas, J. P. B. Silva, K. Kamakshi, N. Dabra, K. C. Sekhar, J. A. Moreira, and M. J. M. Gomes, Ceram. Int. **45**, 5808 (2019).

[45] D. A. Ochoa, A. R. Montero, F. Suñol, M. E. V. Castrejón, L. Pardo, and J. E. García, J. Alloys Compd. **774**, 410 (2019).

[46] A. B. Swain, D. Murali, B. R. K. Nanda, and P. Murugavel, Phys. Rev. Appl. **11**, 044007 (2019).

[47] A. Mondal, P. Saha, B. Ghosh, M. Sahu, G. D. Mukherjee, R. Ranjan, and K. Brajesh, J. Am. Ceram. Soc. **103**, 5259 (2020).

[48] Y. Yang, W. Wang, X. Chen, Y. Wang, D. Gao, and D. Xue, J. Mater. Sci. **55**, 16890 (2020).

[49] K. Dey, A. Ahad, K. Gautam, A. Tripathy, S. S. Majid, S. Francoual, C. Richter, M. N. Singh, A. Sagdeo, E. Welter, N. Vittayakorn, V. G. Sathe, R. Rawat, and D. K. Shukla, Phys. Rev. B **103**, L100205 (2021).

[50] M. Acosta, N. Novak, G. A. Rossetti, and J. Rödel, Appl. Phys. Lett. **107**, 142906 (2015).

[51] J. Gao, X. Hu, L. Zhang, F. Li, L. Zhang, Y. Wang, Y. Hao, L. Zhong, and X. Ren, Appl. Phys. Lett. **104**, 252909 (2014).

[52] M. Acosta, N. Khakpash, T. Someya, N. Novak, W. Jo, H. Nagata, G. A. Rossetti, and J. Rödel, Phys. Rev. B **91**, 104108 (2015).

[53] Y. Nahas, A. Akbarzadeh, S. Prokhorenko, S. Prosandeev, R. Walter, I. Kornev, J. Íñiguez, and L. Bellaiche, Nat. Commun. **8**, 15944 (2017).

[54] K. Datta, K. Brajesh, R. Ranjan, and B. Mihailova, Phys. Rev. B **102**, 060102(R) (2020).

[55] S. Dash, H. S. Mohanty, K. Bhoi, R. Kant, A. Kumar, R. Thomas, and D. K. Pradhan, J. Mater. Sci. Mater. Electron. **29**, 20820 (2018).

[56] J. P. Perdew, K. Burke, and M. Ernzerhof, Phys. Rev. Lett. **77**, 3865 (1996).

[57] G. Kresse and J. Furthmüller, Phys. Rev. B **54**, 11169 (1996).

[58] G. Kresse and D. Joubert, Phys. Rev. B **59**, 1758 (1999).

[59] P. E. Blöchl, Phys. Rev. B **50**, 17953 (1994).

[60] C. Cazorla and M. Stengel, Phys. Rev. B **90**, 020101(R) (2014).

[61] C. Cazorla and M. Stengel, Phys. Rev. B **92**, 214108 (2015).

[62] C. Cazorla and J. Íñiguez, Phys. Rev. B **88**, 214430 (2013).

[63] C. Cazorla, O. Diéguez, and J. Íñiguez, Sci. Adv. **3**, e1700288 (2017).

[64] M. Abebe, K. Brajesh, A. Mishra, A. Senyshyn, and R. Ranjan, Phys. Rev. B **96**, 014113 (2017).

[65] S. P. Singh, R. Ranjan, A. Senyshyn, D. Trots, and H. Boysen, J. Phys. Condens. Matter **21**, 375902 (2009).

[66] M. M. Rahaman, T. Imai, T. Sakamoto, S. Tsukada, and S. Kojima, Sci. Rep. **6**, 23898 (2016).

[67] M. M. Rahaman, T. Imai, T. Sakamoto, M. A. Helal, S. Tsukada, and S. Kojima, J. Alloys Compd. **735**, 1063 (2018).

[68] N. K. Karan, R. S. Katiyar, T. Maiti, R. Guo, and A. S. Bhalla, J. Raman Spectrosc. **40**, 370 (2009).

[69] M. DiDomenico Jr, S. H. Wemple, S. P. S. Porto, and R. P. Bauman, Phys. Rev. **174**, 522 (1968).

[70] G. Burns and B. A. Scott, Solid State Commun. **9**, 813 (1971).

[71] P. Hermet, M. Veithen, and P. Ghosez, J. Phys. Condens. Matter **21**, 215901 (2009).

[72] K. Laabidi, M. D. Fontana, and B. Jannot, Solid State Commun. **76**, 765 (1990).

[73] N. V. Dang, T. D. Thanh, L. V. Hong, V. D. Lam, and T.-L. Phan, J. Appl. Phys. **110**, 043914 (2011).

[74] C. J. Xiao, C. Q. Jin, and X. H. Wang, Mater. Chem. Phys. **111**, 209 (2008).

[75] E. Buixaderas, M. Berta, L. Kozielski, and I. Gregora, Phase Transitions **84**, 528 (2011).

[76] G. Singh, V. Sathe, and V. S. Tiwari, J. Electron. Mater. **46**, 4976 (2017).

[77] I. G. Siny, R. Tao, R. S. Katiyar, R. Guo, and A. S. Bhalla, J. Phys. Chem. Solids **59**, 181 (1998).

[78] U. Fano, Phys. Rev. **124**, 1866 (1961).

[79] D. L. Rousseau and S. P. S. Porto, Phys. Rev. Lett. **20**, 1354 (1968).

[80] A. Pinczuk, E. Burstein, and S. Ushioda, Solid State Commun. **7**, 139 (1969).

[81] J. -H. Ko, T. H. Kim, K. Roleder, D. Rytz, and S. Kojima, Phys. Rev. B **84**, 094123 (2011).

[82] M. D. Fontana, N. Kokanyan, and T. H. Kauffmann, J. Phys. Condens. Matter **32**, 285403 (2020).

[83] S. Banerjee, D. -I. Kim, R. D. Robinson, I. P. Herman, Y. Mao, and S. S. Wong, Appl. Phys. Lett. **89**, 223130 (2006).

[84] D. K. Pradhan, H. S. Mohanty, S. Kumari, K. Bhoi, N. Tang, M. M. Rahaman Ravikant, D. K. Pradhan, A. Kumar, D. A. Gilbert, and P. D. Rack, J. Mater. Chem. C **9**, 12694 (2021).

[85] G. Burns and B. A. Scott, Phys. Rev. B **7**, 3088 (1973).

[86] M. M. Rahaman, T. Imai, T. Sakamoto, and S. Kojima, Integr. Ferroelectr. **185**, 22 (2017).

[87] F. R. -Marcos, A. D. Campo, P. Marchet, and J. F. Fernández, Nat. Commun. **6**, 6594 (2015).

[88] D. H. Suh, D. H. Lee, and N. K. Kim, J. Eur. Ceram. Soc. **22**, 219 (2002).

[89] X. G. Tang, K. H. Chew, and H. L. W. Chan, Acta Mater. **52**, 5177 (2004).

[90] K. Uchino and S. Nomura, Ferroelectrics **44**, 55 (1982).

[91] G. D. Adhikary, D. K. Khatua, A. Mishra, A. De, N. Kumar, S. Saha, U. Shankar, A. Senyshyn, B. N. Rao, and R. Ranjan, Phys. Rev. B **100**, 134111 (2019).

[92] R. E. Eitel, C. A. Randall, T. R. Shrout, P. W. Rehrig, W. Hackenberger, and S.-E. Park, Jpn. J. Appl. Phys. **40**, 5999 (2001).

[93] A. A. Bokov and Z. G. Ye, Phys. Rev. B **65**, 144112 (2002).

[94] R. Pandey, B. Narayan, D. K. Khatua, S. Tyagi, A. Mostaed, M. Abebe, V. Sathe, I. M. Reaney, and R. Ranjan, Phys. Rev. B **97**, 224109 (2018).

[95] A. B. -Holder, H. Beige, and G. Völkel, Phys. Rev. B **79**, 184111 (2009).

[96] V. V. Shvartsman and D. C. Lupascu, J. Am. Ceram. Soc. **95**, 1 (2012).

[97] B. C. Keswani, D. Saraf, S. I. Patil, A. Kshirsagar, A. R. James, Y. D. Kolekar, and C. V. Ramana, J. Appl. Phys. **123**, 204104 (2018).

[98] C. Zhao, W. Wu, H. Wang, and J. Wu, J. Appl. Phys. **119**, 024108 (2016).

[99] Y. Tian, X. Chao, L. Wei, P. Liang, and Z. Yang, J. Appl. Phys. **113**, 184107 (2013).

[100] M. Zakhozheva, L. A. Schmitt, M. Acosta, H. Guo, W. Jo, R. Schierholz, H. J. Kleebe, and X. Tan, Phys. Rev. Appl. **3**, 064018 (2015).

[101] D. Damjanovic, Appl. Phys. Lett. **97**, 062906 (2010).

[102] M. E. Lines and A. M. Glass, *Principles and Applications of Ferroelectrics and Related Materials* (Oxford University Press, New York, 2001).

[103] H. Fu and R. E. Cohen, Nature (London) **403**, 281 (2000).

[104] F. Li, D. Lin, Z. Chen, Z. Cheng, J. Wang, C. Li, Z. Xu, Q. Huang, X. Liao, L.-Q. Chen, T. R. Shrout, and S. Zhang, Nat. Mater. **17**, 349 (2018).

[105] F. Cordero, F. Craciun, M. Dinescu, N. Scarisoreanu, C. Galassi, W. Schranz, and V. Soprunyuk, Appl. Phys. Lett. **105**, 232904 (2014).

[106] M. Ahart, M. Somayazulu, R. E. Cohen, P. Ganesh, P. Dera, H. Mao, R. J. Hemley, Y. Ren, P. Liermann, and Z. Wu, Nature (London) **451**, 545 (2008).

[107] B. Noheda, Curr. Opin. Solid State Mater. Sci. **6**, 27 (2002).

[108] N. Zhang, H. Yokota, A. M. Glazer, Z. Ren, D. A. Keen, D. S. Keeble, P. A. Thomas, and Z. G. Ye, Nat. Commun. **5**, 5231 (2014).

[109] A. K. Singh and D. Pandey, Phys. Rev. B **67**, 064102 (2003).

[110] D. L. Orauttapong, B. Noheda, Z. G. Ye, P. M. Gehring, J. Toulouse, D. E. Cox, and G. Shirane, Phys. Rev. B **65**, 144101 (2002).

[111] J. Y. Li, R. C. Rogan, E. Üstündag, and K. Bhattacharya, Nat. Mater. **4**, 776 (2005).

[112] Z. Kutnjak, J. Petzelt, and R. Blinc, Nature (London) **441**, 956 (2006).

[113] A. Pramanick, D. Damjanovic, J. E. Daniels, J. C. Nino, and J. L. Jones, J. Am. Ceram. Soc. **94**, 293 (2011).